JGR Space Physics

RESEARCH ARTICLE
10.1029/2021JA029565

Key Points:

- Van Allen Probe data are used to create models of electron density and average ion mass
- Models are combined to describe plasma mass density in the magnetic equatorial plane
- Models are parameterized using artificial neural networks

Supporting Information:

Supporting Information may be found in the online version of this article.

Correspondence to:

M. K. James,
mkj13@leicester.ac.uk

Citation:

James, M. K., Yeoman, T. K., Jones, P., Sandhu, J. K., & Goldstein, J. (2021). The Scalable Plasma Ion Composition and Electron Density (SPICED) model for Earth's inner magnetosphere. *Journal of Geophysical Research: Space Physics*, *126*, e2021JA029565. https://doi.org/10.1029/2021JA029565

Received 14 MAY 2021
Accepted 20 AUG 2021

The Scalable Plasma Ion Composition and Electron Density (SPICED) Model for Earth's Inner Magnetosphere

Matthew K. James[1], Tim K. Yeoman[1], Petra Jones[2,3], Jasmine K. Sandhu[4], and Jerry Goldstein[5,6]

[1]Department of Physics and Astronomy, University of Leicester, Leicester, UK, [2]Leicester Diabetes Centre, University Hospitals of Leicester, Leicester General Hospital, Leicester, UK, [3]Diabetes Research Centre, University of Leicester, Leicester General Hospital, Leicester, UK, [4]Northumbria University, Newcastle, UK, [5]Space Science and Engineering Division, Southwest Research Institute, San Antonio, TX, USA, [6]Department of Physics and Astronomy, University of Texas at San Antonio, San Antonio, TX, USA

Abstract The plasma mass loading of the terrestrial equatorial inner magnetosphere is a key determinant of the characteristics and propagation of ultra low frequency waves. Electron number density is also an important factor for other types of waves such as chorus, hiss and EMIC waves. In this paper, we use Van Allen Probe data from September 2012 to February 2019 to create average models of electron densities and average ion mass in the plasmasphere and plasmatrough, near the Earth's magnetic equator. These models are combined to provide an estimate of the most probable plasma mass density in the equatorial region. We then use machine learning to form a set of models which are parameterized by the SuperMAG ring current index based on the design of the average models. The resulting set of models are capable of predicting the average ion mass, electron density and plasma mass density in the range $2 \leq L \leq 5.9$ and over all magnetic local time sectors during a range of conditions where $-75 \leq SMR \leq +27$ nT.

1. Introduction

Plasma mass density is an important consideration for magnetospheric physics because it affects the timescales over which magnetospheric processes occur such as magnetic reconnection, by changing plasma β (e.g., Phan et al., 2013); and ultra low frequency (ULF) wave propagation speeds (e.g., Alfvén, 1942). In this paper, we use Van Allen Probe, formerly Radiation Belt Storm Probes (RBSP), (Mauk et al., 2013) data to characterize the plasma mass density close to the Earth's magnetic equatorial plane within the inner magnetosphere.

Energy and momentum are transmitted throughout a magnetized plasma, such as that of the Earth's magnetosphere, via the propagation of magnetohydrodynamic (MHD) waves. The characteristic propagation speed of such waves is the Alfvén velocity: $v_A = \frac{B}{\sqrt{\mu_0 \rho}}$, which depends on both the magnetic field magnitude, B, and the plasma mass density ρ, where μ_0 is the permeability of free space. In a cold plasma, there are two MHD modes: the "fast" magnetosonic mode and the "Alfvén" mode. The fast mode is a compressional wave, which may propagate isotropically both along and across the magnetic field with a phase speed equal to v_A. Unlike the fast magnetosonic mode, the Alfvén mode is a transverse, field-guided wave, also with a velocity equal to v_A - this means that on closed magnetospheric flux tubes standing Alfvén waves can exist, where the Alfvén wave is reflected at each end of the flux tube by the highly conductive ionosphere. Much like the waves on a guitar string, Alfvén waves standing on closed field lines have discrete eigenfrequencies which are determined by field line length, magnetic field strength and plasma mass density (e.g., Goldstein et al., 1999) (analogous to string length, tension and thickness).

Due to the contribution of plasma mass density to determining Alfvén wave speeds, it is crucial to be able to reliably describe the complexity and variability of plasma mass density in the inner magnetosphere. The plasma in Earth's inner magnetosphere is highly structured, with the cold, high density (>100 cm^{-3}) plasmaspheric population occupying low L values, the more tenuous (<10 cm^{-3}) plasmatrough population

existing at higher L values, and the plasmapause boundary separating the two. Whereas the plasmapause originates predominantly from the interplay of ionospheric refilling and erosion, the plasmatrough contains plasma from both direct ionospheric outflows as well as convected plasma from the plasma sheet. In terms of loss processes, the dominant contributor is convective erosion. Flux tubes undergoing convective flows experience dramatic plasma loss following reconnection at the dayside magnetopause, where this process is attributed to the sharp drop in density outside the plasmapause (Chappell, 1972). During periods of enhanced magnetospheric convection (e.g., geomagnetic storms), convection erosion is increased and can significantly erode the plasmapause to low L values (Darrouzet et al., 2009). Furthermore, enhanced heavy ion outflows during active periods can radically alter the mass density of inner magnetospheric plasma (Kronberg et al., 2014; Sandhu et al., 2017).

A number of models of electron and ion densities have been produced using in-situ data (e.g., Carpenter & Anderson, 1992; Gallagher et al., 1988, 2000). Carpenter and Anderson (1992) used ISEE (International Sun-Earth Explorer) 1 data to produce a model of electron density in the region $2.25 < L < 8$, although the coverage in magnetic local time (MLT) was limited to the range 0–15 h due to the variable plasma structure in the evening sector. Another model of electron densities by Sheeley et al. (2001) used CRRES measurements to model both the plasmasphere and plasmatrough for all local times and L-shells in the range $3 < L < 7$—this model did not include any dependence on magnetic activity. A model of proton densities was also produced using data from the Dynamics Explorer 1 satellite (Gallagher et al., 1988) which used an analytical expression to describe plasmaspheric and plasmapause proton densities during moderate geomagnetic activity. The Global Core Plasma Model (GCPM) (Gallagher et al., 2000), is notable in that it provided both electron density and ion composition information parameterized by solar and geomagnetic activity, and was a combination of separate models for the ionosphere, plasmasphere, plasma trough, plasmapause and the polar cap.

More recently, machine learning has been utilized to form electron density models; Zhelavskaya et al. (2017) created the PINE (Plasma density in the Inner magnetosphere Neural networks-based Empirical)–an artificial neural network-based model using Van Allen Probe measurements of electron density. This model is capable of reproducing the cold electron dynamics of the equatorial inner magnetosphere and compares well with IMAGE extreme ultraviolet (EUV) images of helium ion column density. Unfortunately, the design of the PINE model is such that there is a discontinuity in the electron densities around midnight and the model itself is not publicly available. Another model of electron density was created by Chu et al. (2017), called the DEN3D (three-dimensional dynamic electron density) model using electron densities measured by a number of different spacecraft. This model used an artificial neural network to predict electron densities in the region $2 \leq L \leq 7$ and is capable of reproducing 91% of measurements. Both PINE and DEN3D models attempt to describe the plasmaspheric and plasmatrough electron densities together, but neither is quite able to accurately depict the relatively sudden transitions between each population across the plasmapause; instead the transition is gradual–effectively smoothing the densities of the two populations together. In this paper, the plasmasphere and plasmatrough populations are considered separately, where a probability model suggests which population is most likely to exist at a given position near the equatorial plane. This configuration allows the predictions of both populations' densities to be predicted independently and, either using the probability model or in-situ observations, the user can decide which is most likely.

In the Earth's magnetosphere, a function based on the position along a field line is sometimes used to describe the distribution of plasma mass density, one example is the power law used by Cummings et al. (1969), where different power law indices were shown to result in changes to both the field line eigenfrequencies and the the ratios of harmonic frequencies. Later work by Denton et al. (2001); Denton et al. (2004) using ULF waves to probe field line mass loading suggested that on more distant field lines, the power law was not completely appropriate to describe observed ULF waves, and that there was an equatorial enhancement in ρ.

Work by Sandhu et al. (2016a), (2016b) used data from the Cluster mission from the outer magnetosphere to construct models of average ion mass and electron density, respectively. The average ion mass, m_{av}, model of Sandhu et al. (2016b) was constructed using CODIF (ion Composition and Distribution Function analyzer, Rème et al., 1997) data, which were used to determine m_{av0}, the equatorial m_{av}, and the variation of m_{av}

along closed field lines within the range of $5.9 < L < 9.5$. This model used a simple power law of the form (e.g., Cummings et al., 1969; Radoski & Carovillano, 1966)

$$m_{av} = m_{av0} R_{norm}^{-\gamma}, \tag{1}$$

where R_{norm} is the normalized radius along the field line, calculated by dividing the radial distance of a given point along a field line from the center of the Earth by the farthest point along that same field line; γ is the power law index, which was determined to vary depending on the L-shell of the field line and the magnetic local time (MLT).

The electron density (n_e) model of Sandhu et al. (2016a) was constructed using electron density obtained from WHISPER (Waves of High frequency and Sounder for Probing of Electron density by Relaxation), (Décréau et al., 1997), measurements of the upper hybrid frequency. This model used a similar approach to that of Sandhu et al. (2016b), where an equatorial electron density, n_{e0}, was determined, as well as the variation of n_e along closed field lines in the region $4.5 < L < 9.5$. This model differed from that of the m_{av} model in that a Gaussian function was used to describe an enhancement in n_e near to the magnetic equator (similar to the mass density functions found by Denton et al. [2004] and Takahashi et al. [2004]), and a power law away from the equator:

$$n_e = \begin{cases} n_{e0} R_{norm}^{-\alpha}, & R_{norm} \leq 0.8 \\ a \exp\left[-\frac{1}{2} \left(\frac{R_{norm} - 1.0}{0.1} \right)^2 \right] + n_{e0}, & R_{norm} > 0.8 \end{cases} \tag{2}$$

where α is the power law exponent and a is the magnitude of the equatorial n_e enhancement, where both a and α are functions of L-shell and MLT. WHISPER is a resonance sounder that determines the electron plasma density to be inferred from measurements of the electron plasma frequency (Trotignon et al., 2001, 2003). The frequency range of the WHISPER instrument restricts measurements of electron density to within 0.25–80 cm^{-3}. Therefore, the Sandhu et al. (2016a) model of electron density mostly represents the plasmatrough population.

Both of the models were later updated such that they were parameterized by the D_{st} index (Sandhu et al., 2017), and when combined they could provide an estimate of the plasma mass density ($\rho = m_{av} n_e$, assuming plasma quasi-neutrality, singly charged ions) within the region where the models overlap.

The aim of this study is to use Van Allen Probe measurements of both electron density and ion composition to complement the models of Sandhu et al. (2016b); Sandhu et al. (2016a, 2017) by modeling n_e and m_{av} in the region where $L < 5.9$. First, a set of models which characterize the average plasma properties is created using the entire data set. Then, by splitting the data into smaller samples the average models are adapted using artificial neural networks to form a set of parameterized models which are driven by the prevailing geomagnetic and solar activity. Analysis of variance (ANOVA) techniques are used to determine which solar wind/geomagnetic parameters are most correlated with changes in electron densities and average ion masses (see section Appendix B). The models are all driven by the SuperMAG ring current index (SMR, Newell & Gjerloev, 2012) provided by SuperMAG (Gjerloev, 2012), where the SMR index is a measure of the horizontal deviation of the Earth's equatorial magnetic field in response to changes to the ring current with a 1-min time resolution–much like the *Dst* (1-h resolution) and SYM-H indices.

2. Data

The models of electron density and average ion mass in the near-equatorial region of the Earth's inner magnetosphere are made using data from both Van Allen Probes, A and B, from September 2012 to October 2019. Both spacecraft exist in a highly elliptical geocentric orbit, close to the equator; each orbit has a duration of ~9h where perigee and apogee are ~1.1 and 5.8 R_E, respectively.

For the electron density model, level 4 data are used from the Electric and Magnetic Field Instrument Suite and Integrated Science (EMFISIS, (Kletzing et al., 2013)) onboard the Van Allen Probes. In the level 4 data set, the electron density, n_e, is calculated with a time resolution of ~6 s using observations of the upper hybrid frequency, f_{uh}, made by the high-frequency receiver of EMFISIS. The upper hybrid frequency is related to the electron cyclotron frequency, f_{ce}, and the electron plasma frequency, f_{pe}, by

$$f_{uh}^2 = f_{ce}^2 + f_{pe}^2. \tag{3}$$

Using direct measurements of the local magnetic field magnitude, B, the electron cyclotron frequency can be determined using

$$f_{ce} = \frac{eB}{2\pi m_e}, \tag{4}$$

where e and m_e are the charge and mass of an electron, respectively. Given the measurements of f_{uh} and f_{ce}, the f_{pe} can be calculated using Equation 3. Finally, the electron density is calculated using

$$n_e = m_e \epsilon_0 \left(\frac{2\pi f_{pe}}{e} \right)^2, \tag{5}$$

where ϵ_0 is the permittivity of free space.

To create the model of average ion mass, the Helium Oxygen Proton and Electron (HOPE) (Funsten et al., 2013) spectrometer, part of the Energetic Particle, Composition, and Thermal Plasma (ECT) suite (Spence et al., 2013), is used to provide measurements of local plasma ion densities. HOPE measures electron and ion fluxes over a wide energy range of 1 eV–50 keV using 72 log-spaced energy bins, capable of detecting ring current plasma and ionospheric outflows. The HOPE cold ion moments are calculated by integrating the low energy portion of the spectra ($E < 20\,eV$) using the methods developed by Goldstein et al. (2014); Genestreti et al. (2017); Goldstein et al. (2019) (see section Appendix A for more information). The Goldstein et al. (2019) method for providing upper and lower limits to the oxygen densities used here effectively adjusts the oxygen density measurements by a constant factor, so should be considered a potential source of error. The ion densities measured using HOPE are used to determine an average ion mass,

$$m_{av} = \frac{\sum m_i n_i}{\sum n_i}, \tag{6}$$

where n_i and m_i are the local number density and mass (in amu) of ion species i, respectively.

3. Models

In this section, the following five models are constructed:

1. A model of the probability of being in the plasmasphere (PS) or plasmatrough (PT) (Section 3.1),
2. Plasmatrough and plasmasphere electron density models (Section 3.2),
3. Plasmatrough and plasmasphere average ion mass models (Section 3.3)

which will be referred to as the P model; n_ePT and n_ePS models; and the m_{av}PT and m_{av}PS models, respectively, throughout this paper. Collectively the models will be called the Scalable Plasma Ion Composition and Electron Density (SPICED) model.

All five models use Van Allen Probe data collected from a region close to the magnetic equatorial plane where $R_{norm} \geq 0.95$, and can be combined to form an overall average equatorial plasma mass density model, using the assumption of plasma quasi-neutrality and most ions being singly charged. The condition $R_{norm} \geq 0.95$ is satisfied by the Van Allen Probes ~70% of the time, and corresponds approximately to magnetic latitudes $|\theta| \leq 13°$. It is also assumed that contributions from other ions (such as N^+) are negligible and the HOPE average ion mass measurements made using the energy range 1–20 eV with the Goldstein et al. (2019) correction are representative of the bulk of the cold magnetospheric plasma. Sandhu et al. (2016b) showed that average ion masses determined in the plasmatrough using Cluster data in a similar energy range (0.7–25 eV) were consistent with m_{av} measurements made using data from a higher energy range (0.025–40 keV).

Each model was constructed by placing data into thin L-shell bins 0.1 wide, each overlapping the next by 0.09, in the interval where $2 \leq L \leq 5.9$. The axisymmetric component (constant for all MLT) of the data was removed before computing the spatial Lomb-Scargle periodogram (L-S) (Lomb, 1976; Scargle, 1983) for each L bin and N_m different azimuthal wavenumbers, m, where the azimuthal wavenumber corresponds to the number of full wave periods it would take to encircle the planet once. The method produces an amplitude, a_{mL}, for each m and L combination. The method described by Hocke (1998) was also used to estimate the phase, ϕ_{mL}, of the azimuthal variations for every wave number.

The model for a parameter, F, was then constructed using a Fourier series,

$$F(L,T) = F_0(L) + \sum_{m=1}^{N_m} A_m(L)\cos\left(2\pi\frac{m}{24}T + \Phi_m(L)\right), \tag{7}$$

where $F_0(L)$ is a function which describes the variations in the axisymmetric component (i.e., $m = 0$) of the parameter F with L, and T is the local time in hours. $A_m(L)$ and $\Phi_m(L)$ are functions which provide the amplitude and phase, respectively, for each azimuthal wavenumber.

Equivalently, Equation 7 can be expressed in its sine-cosine form,

$$F(L,T) = F_0(L) + \sum_{m=1}^{N_m}\left\{R_m(L)\cos\left(2\pi\frac{m}{24}T\right) + I_m(L)\sin\left(2\pi\frac{m}{24}T\right)\right\}, \tag{8}$$

where

$$A_m(L) = \sqrt{R_m(L)^2 + I_m(L)^2}, \tag{9}$$

$$\Phi_m(L) = \arctan 2\left(\frac{I_m(L)}{R_m(L)}\right). \tag{10}$$

$R_m(L)$ and $I_m(L)$ are polynomial functions fitted to the real and imaginary Fourier coefficients obtained using the Lomb-Scargle analysis. In order to fit the function $\Phi_m(L)$ directly to the phases output by the L-S analysis of each L bin, the phases would require unwrapping first. Using the sine-cosine form of the Fourier series with $R_m(L)$ and $I_m(L)$ instead of the amplitude-phase form in Equation 7 means that no phases need to be unwrapped. This is particularly useful in the case of the models presented later in Section 4.3, where we can avoid the complexity and unreliability of 2D phase-unwrapping algorithms.

3.1. Probability (P) Model

The first step in creating the probability model was to separate electron density measurements by the plasma population from which they originated. Measurements were separated using (Sheeley et al., 2001),

$$n_b = 10\left(\frac{6.6}{L}\right)^4, \tag{11}$$

where L is the L-shell of the spacecraft at the time of the observation. Measurements where $n_e > n_b$ were considered to originate from the plasmaspheric population, otherwise they are considered to be from the plasmatrough. The reliability of using this equation for the classification of electron density measurements is discussed in Section 3.2.

The axisymmetric component of the probability model, P_0, was found by placing data from all local times into thin L bins and calculating the probability using,

$$P = \frac{N_{PS}}{N_{PS} + N_{PT}}, \tag{12}$$

where N_{PS} is the number of plasmaspheric measurements and N_{PT} is the number of plasmatrough measurements. Figure 1 shows P_0 as a function of L in black, with a fitted variant of the logistic function similar to the sigmoid function,

$$P_0(L) = \frac{-1}{1 + \exp^{-a(L-b)}} + 1, \tag{13}$$

is shown as a red dashed line, where a and b are free parameters. This form of the logistic function was used because it is constrained such that it could only take values in the range $0 < P_0 < 1$, where parameter a controls the rate of change in P_0 with L and parameter b controls where in L the function crosses the $P_0 = 0.5$ threshold occurs. For the fitted functions shown in Figure 1,the parameters a and b were found numerically using the downhill-simplex method (Nelder & Mead, 1965) (all model parameters are available in the Data Set S1; model code is also available at https://github.com/mattkjames7/spicedmodel).

The next stage in forming this part of the model was to perform L-S analysis on the data; this was achieved by assigning the value of 1 to each PS measurement, and 0 to PT measurements and then subtracting P_0 prior to using the L-S method. Figure 2 shows the R_m (a) and I_m (b) parameters output from the L-S analysis as

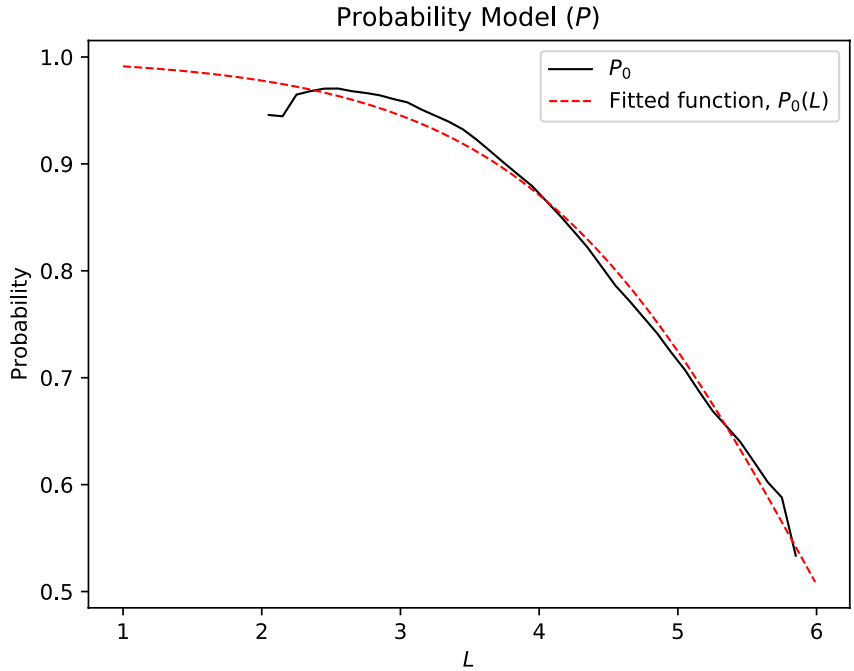

Figure 1. Axisymmetric component of the probability model as a function of L in black, with a fitted logistic function shown as a red dashed line.

a function of L for the first three m numbers from 1 to 3 (red, yellow and cyan, respectively). In both panels, the dashed lines correspond to the fitted 3^{rd}-order polynomial functions $R_m(L)$ and $I_m(L)$.

Figure 3 shows the probability model in the equatorial plane, where (a) is the axisymmetric portion of the model, (b) is the spatial variation due to the periodic components of the model and (c) is the combined model. The color scale used in panels (a) and (c) is such that red corresponds to positions which are more likely to be within the plasmasphere ($P > 0.5$); blue would suggest that the plasmatrough is more likely; and white regions suggest that the probability of encountering either plasma population is close to being equal ($P \approx 0.5$). Panel (b) shows the spatial variations due to the periodic components of the model, where red implies a local increase in P (with solid contour lines) and blue means a reduction in P (dashed contour lines).

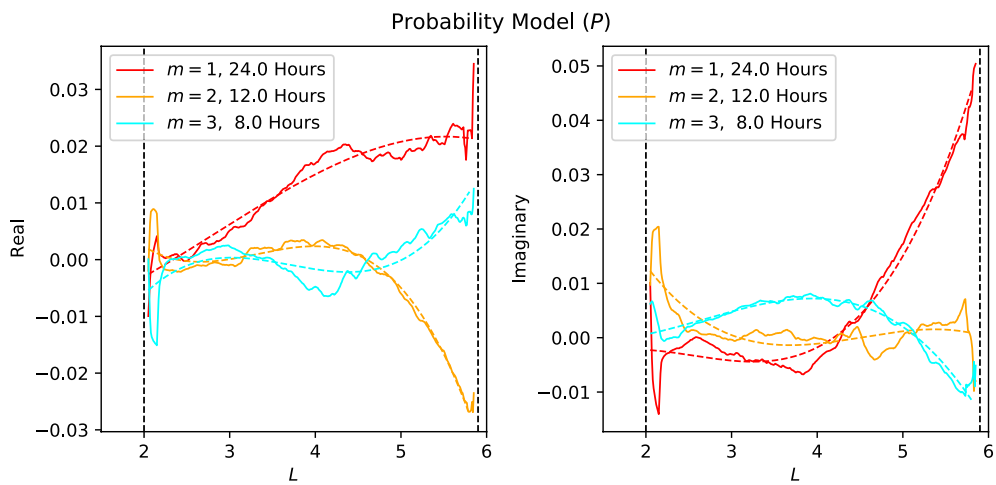

Figure 2. Real (panel a) and imaginary (panel b) components of the L-S periodogram as a function of L for the first three integer values of m. Dashed lines show fitted third-order polynomials corresponding each component and m number.

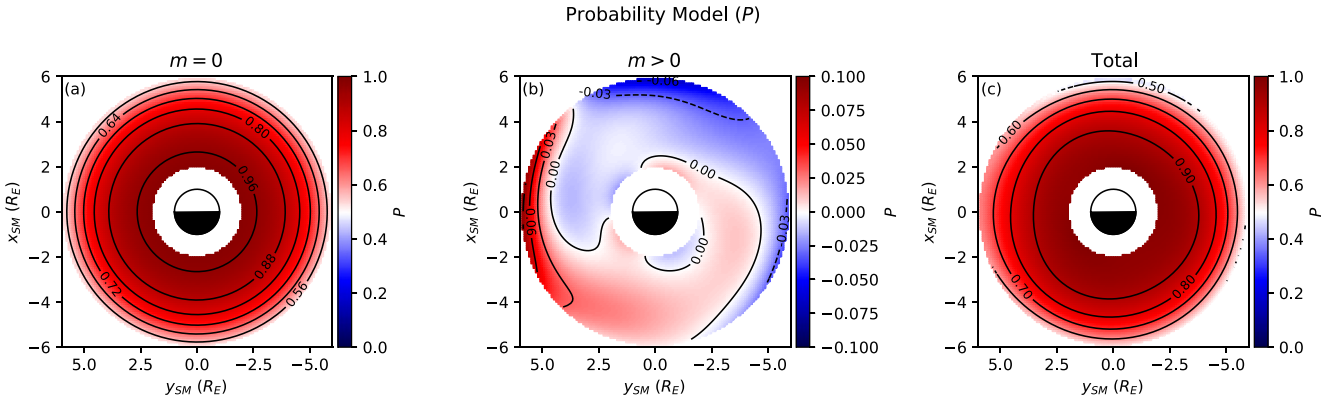

Figure 3. Panel (a) shows the axisymmetric component of the model in the equatorial plane, while panel (b) shows the spatial variations in the probability model and panel (c) shows the sum of both. All three panels are arranged such that noon is at the top and dawn is on the right. The color scale in panels (a) and (c) are such that red regions correspond to where $P > 0.5$ (most likely to be inside the PS), blue regions are most likely to be PT and white regions $P \approx 0.5$ could be considered to be a likely location for an average plasmapause. Panel (b) is colored based on the spatial variations in P provided by the L-S analysis; red areas act to increase the overall value of P, while blue regions reduce the overall value of P. Contours are shown in black in each panel, where negative variations in panel b are represented by dashed contours.

Figures 1 and 3 show that overall the plasmasphere is considerably more likely to be encountered within the region $2 \leq L \leq 5.9$, generally with $P > 0.5$. At larger L, where Figure 3c is mostly white, P is close to 0.5 so either population could be present. The spatial variations presented in Figure 3b suggest that there is an asymmetry, with an increased probability (up to ~10%) of being in the plasmasphere around dusk at $L > 5$. Figure 3c also suggests that the plasmatrough is more commonly observed at larger L in the noon sector.

The probability model presented here is created using all data, and is therefore considered to be an average picture of the probability of any position within this region being within the plasmasphere. The plasmasphere undergoes significant changes in shape and size depending upon the global magnetospheric state (e.g., Moldwin et al., 2002; Spasojević et al., 2003), so a parameterized version of this model which can exhibit much of this variation is presented later, in Section 4.3.

3.2. Plasmatrough (n_ePT) and Plasmasphere (n_ePS) Electron Density Models

The n_ePT and n_ePS models are both created in a similar way to the probability model, by subtracting some axisymmetric component which does not vary with azimuth, and then using L-S to determine the amplitudes and phases of variations which occur with integer values of m. Figure 4a shows a histogram of the n_e measurements used to create these models; n_e is not distributed normally (as a Gaussian) and can take

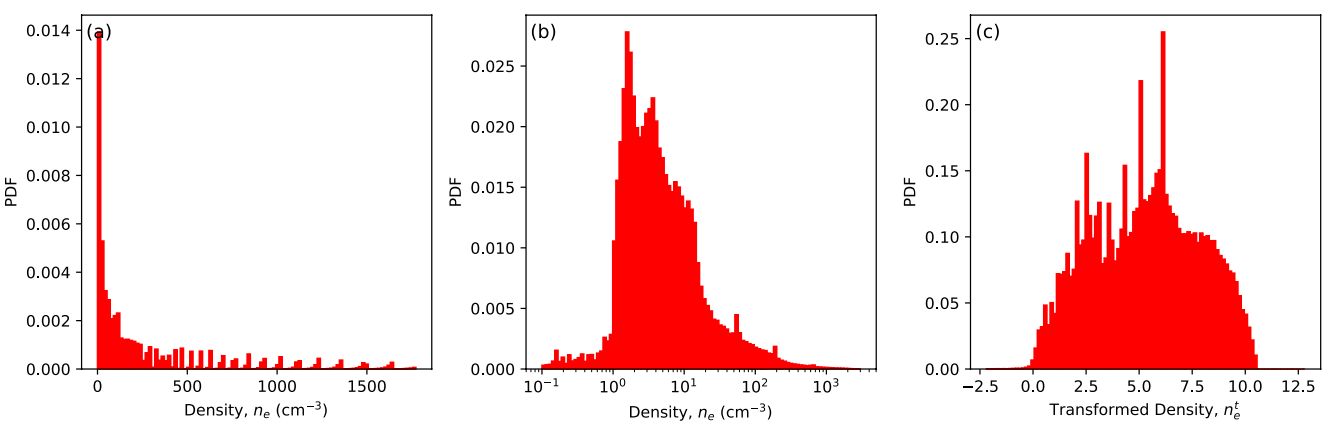

Figure 4. In panel (a), histogram showing the distribution of all n_e measurements as probability density. Panel (b) shows the distribution of $\log_{10} n_e$. Panel (c) shows the probability density histogram of n_e^t.

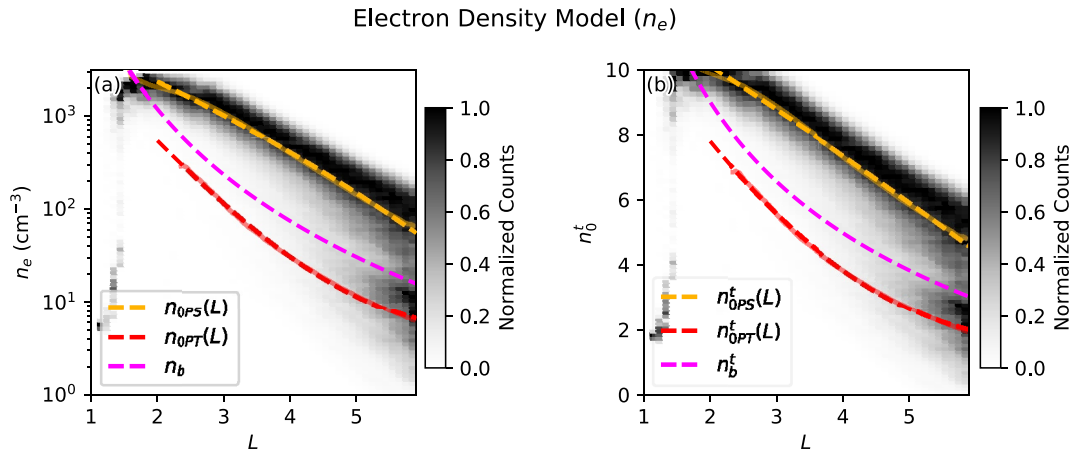

Figure 5. The distribution of electron density, n_e, panel (a) and Box-Cox transformed density, n_e^t, panel (b) against L -shell near the magnetic equatorial plane. The color scale used represents the "normalized counts," where each column is scaled between 0 and 1. The solid red and yellow lines show the mean values of n_e^t for the plasma trough and the plasmasphere, respectively, where dashed lines show polynomial fits to those means. In both panels, the pink dashed line represents n_b from Equation 11.

values over a range of different orders of magnitude. The result of this highly non-Gaussian distribution is that the mean of n_e in a L bin will not accurately represent the expected value of n_e. Figure 4b shows that $\log_{10} n_e$ is much closer to being normally distributed, but a better (more Gaussian) solution to this problem is the use the Box-Cox transformation (Box & Cox, 1964):

$$n_e^t = \begin{cases} \dfrac{n_e^\lambda - 1}{\lambda}, & \text{if } \lambda \neq 0 \\ \log n_e & \text{if } \lambda = 0 \end{cases} \tag{14}$$

where λ is the power parameter, n_e must be greater than zero, and n_e^t is the transformed electron density. The value of λ was obtained by maximizing the log-likelihood function (e.g., Box & Cox, 1964),

$$f(n_e, \lambda) = -\frac{N}{2}\log\left[\sum_{i=1}^{N}\frac{(n_{e,i}^t - (\overline{n}_e^t)^2)}{N}\right] + (\lambda - 1)\sum_{i=1}^{N}\log(n_{e,i})$$

where

$$\overline{n}_e^t = \frac{1}{N}\sum_{i=1}^{N} n_{e,i}^{(\lambda)}, \tag{15}$$

and N is the number of n_e measurements. This transforms the distributions of n_e to create the distribution in Figure 4c, which is closer to a normal distribution.

Figure 5a shows the distribution of n_e as measured by EMFISIS versus L, where each column is normalized so that the maximum of each is 1. Panel b of Figure 5 is similar to panel a, except it is showing the histogram of the Box-Cox transformed densities. The pink dashed line represents n_b from Equation 11 which separates the PS densities, n_{ePS}, and the PT densities, n_{ePT}. The axisymmetric component of the model was found by splitting the data into many thin L bins and calculating the mean of the transformed density for each bin in both populations. The mean transformed densities, n_{0PS}^t (yellow) and n_{0PT}^t (red), are presented as solid lines in panel b of Figure 5; the reverse Box-Cox transform of them, n_{ePS} and n_{ePT}, are also presented as solid lines in panel a. The function $n_{dc}(L)$ for each population was then obtained by fitting a 2^{nd}-order polynomial to n_0^t, both of which are presented as dashed lines in panels a and b of Figure 5.

The n_b line in Figure 5 (in pink) was used by Sheeley et al. (2001) to separate the the mean electron density distributions of the plasmasphere and plasmatrough. It was acknowledged by Sheeley et al. (2001) that using Equation 11 to classify the two populations could be a possible source of error due to the potential overlap in the electron density distributions of the two populations. It is also evident from Figure 5 that for low L (< 2), n_b would be greater than the electron densities predicted by extrapolating the PS model, which would lead to relatively high plasmaspheric electron densities (~ 5000 cm^{-3} or more) being mislabeled as

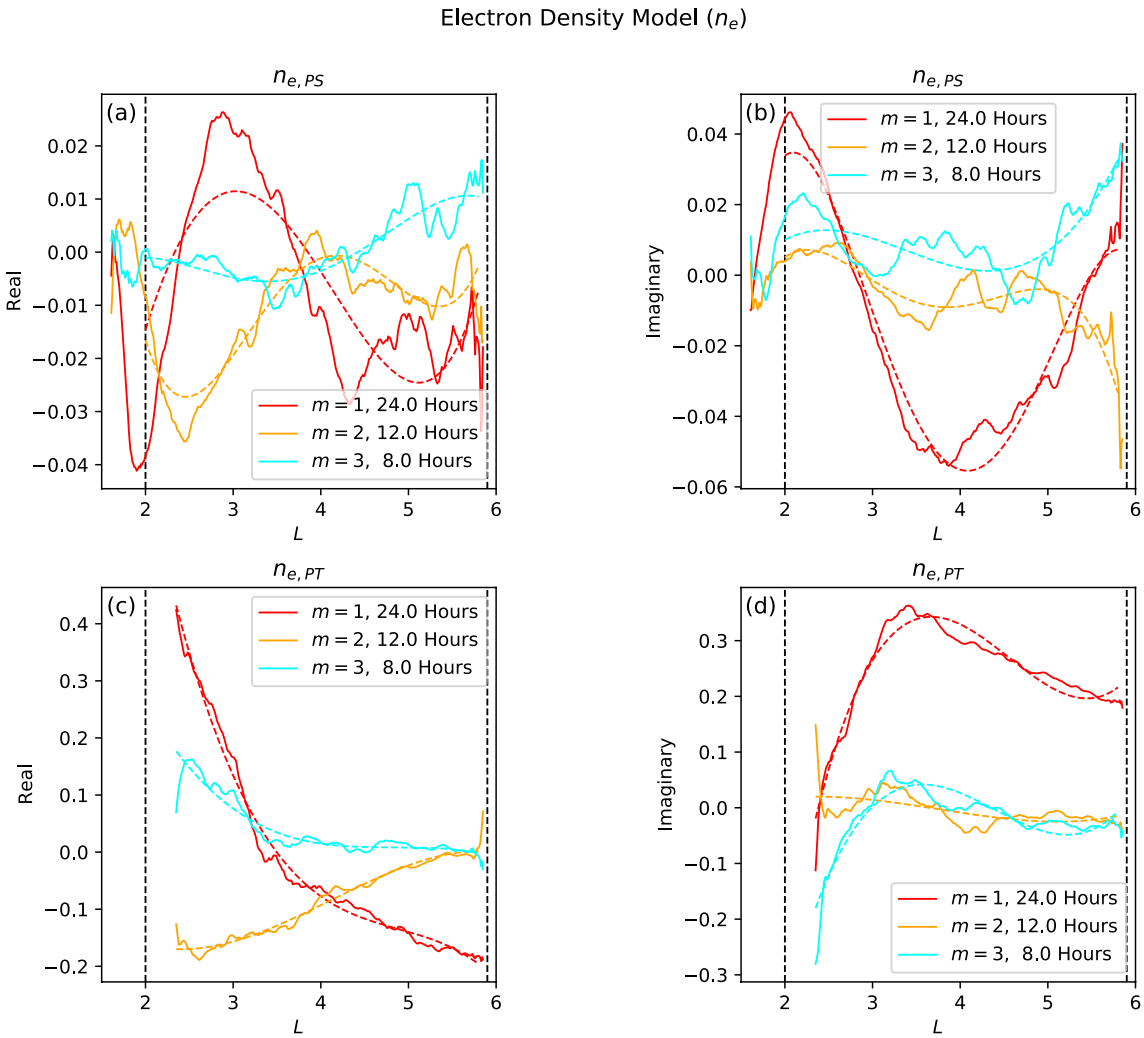

Figure 6. Panels (a) and (c) represent the real parts of the n_ePS and n_ePT models, respectively. Panels (b) and (d) show the imaginary components for the n_ePS and n_ePT models, respectively. These plots are in the same format as those in Figure 2.

plasmatrough densities. Fortunately, in the region of the inner magnetosphere considered here ($2 < L < 5.9$), Figure 5 shows that Equation 11 appears to separate the two populations reliably overall.

As in the probability model, the axisymmetric component of the density was subtracted from the data in each of the L bins for both models so that L-S analysis could be performed. The Real, $R_m(L)$, and the imaginary, $I_m(L)$, functions for both models are presented in Figure 6, where the top panels (a and b) correspond to the PS model, the bottom panels (c and d) are for the PT model, the left panels show $R_m(L)$ and the right panels show $I_m(L)$. The real and imaginary functions were 4^{th}-order polynomial fits for the PS model and 3^{rd} order for the PT model.

Figure 7 shows the axisymmetric contributions to the density models (panels a and b), the percentage difference to the axisymmetric component due to spatially varying contributions (panels c and d) and the total density models (panels e and f). Panels on the left of Figure 6 (panels a, c and e) correspond to the n_ePS model, and those on the right (panels b, d and f) represent the n_ePT model. With the exception of the color scale used, the format of each panel is similar to the equivalents plots in Figure 3.

The axisymmetric components of both n_ePS and n_ePT models behave as expected, where they exhibit a monotonic decrease in density as L increases. Spatial variations in the n_ePS model suggest modest changes in density with local time, the magnitudes of these variations are usually less than 4% of the axisymmetric

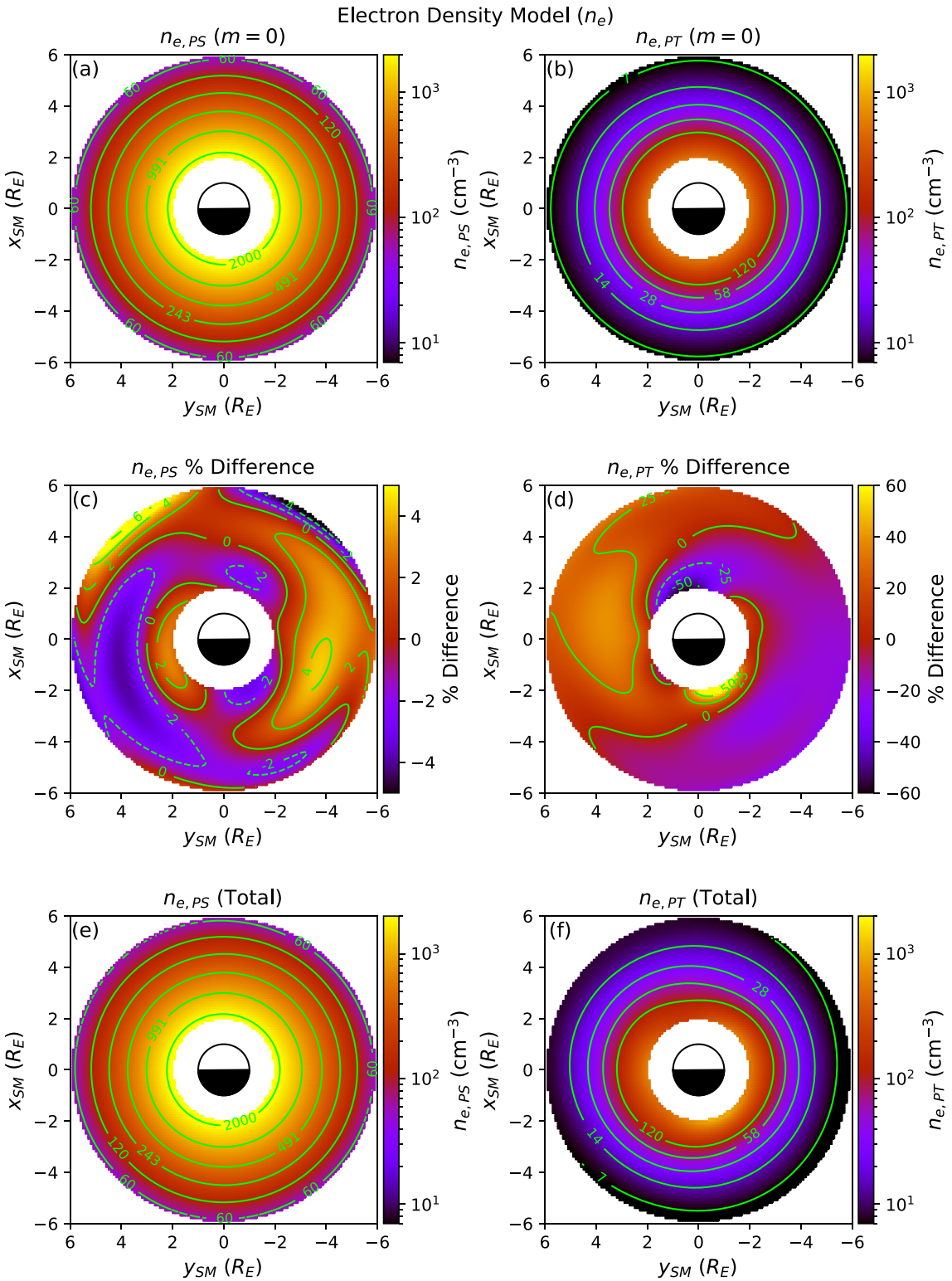

Figure 7. Panels (a) and (b) show the axisymmetric components of the PS and PT n_e models, respectively. Panels (c) and (d) show the percentage difference to the axisymmetric component due to the periodic variations in n_e for both models, where green contour lines are solid for positive variations and dashed for negative variations. Panels (e) and (f) show the combination of the axisymmetric and periodic components to form the PS and PT n_e models, respectively, where contour lines show the effect which the spatial variations have upon the model. All panels are oriented such that noon is at the top and dawn is to the right.

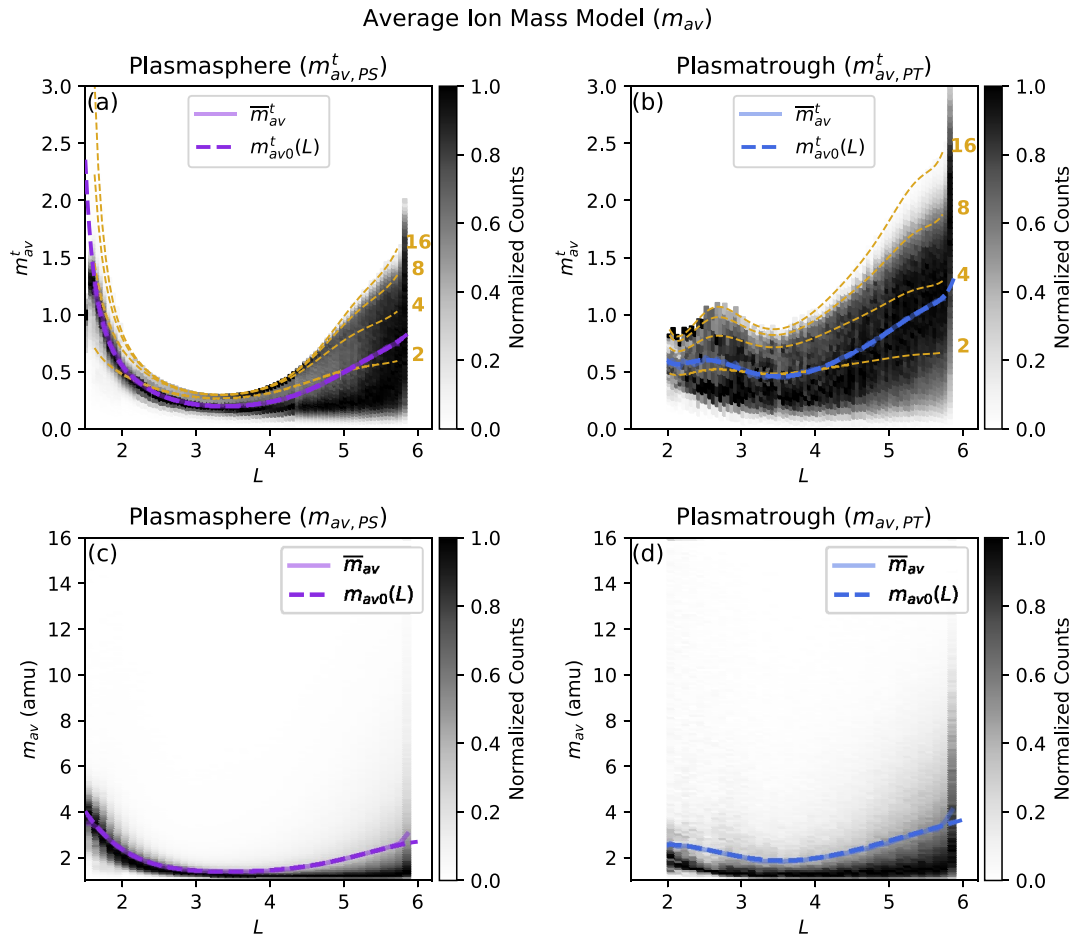

Figure 8. 2D histograms of m^t_{av} panels (a) and (b) and m_{av} panels (c) and (d), in a similar format to that of Figure 5. Panels on the left (a) and (c) correspond to plasmaspheric composition and panels on the right (b) and (d) show the distributions from the plasmatrough population. Solid purple (PS) and blue (PT) lines show the mean m^t_{av} for each L-shell, where the dash lines are polynomial fits to those means. Gold dashed lines in panels a and b show the transformed even integer values of m_{av} from 2 to 14 as a function of L.

component of the model. While there appear to be substantial changes in the density with local time at low L, the same is true about the spatial variations depicted by the PT model, with most being less than 25% of the magnitude of the axisymmetric component.

3.3. Plasmatrough (m_{av}PT) and Plasmasphere (m_{av}PT) Average Ion Mass Models

The average ion mass models are constructed in a very similar way to the electron density models in Section 3.2, where the main difference lies in the transform used on the data. The distribution of m_{av} is highly skewed towards $m_{av} \approx 1$, but the shape of this distribution varies significantly with L. Instead of using a single value of λ in Equation 14 for all values of m_{av}, a smooth polynomial function of L was used for the transform (i.e., $\lambda \rightarrow \lambda(L)$).

Figure 8 shows two pairs of 2D histograms in a similar format to those in Figure 5, where the left panels (a and c) correspond to the plasmaspheric measurements of m_{av} and right panels (b and d) show the distributions of plasmatrough m_{av}. Panels a and b show the transformed distributions of average ion mass (m^t_{av}), where gold dashed lines show the equivalent average ion mass in amu; panels c and d show the distributions of m_{av}. The solid purple and blue lines represent the mean values of m^t_{av} for the plasmasphere and plasmatrough, respectively, where the dashed lines show a polynomial fit.

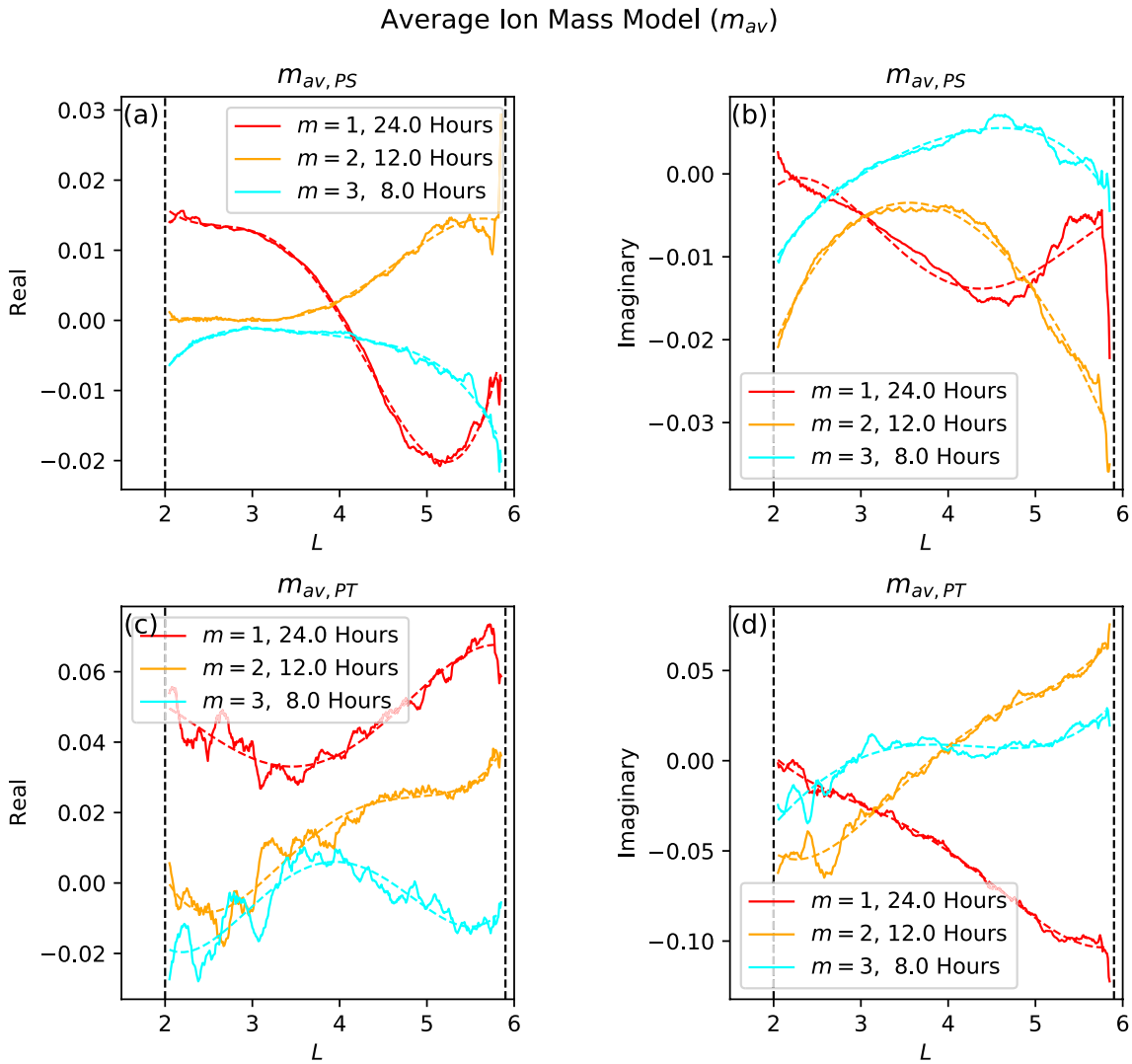

Figure 9. L-S real and imaginary components for the m_{av} model presented in the same format as those in Figures 2 and 6.

Unlike in Figure 5a, where there are two distinct populations of electrons, Figure 8 shows that both populations have similar, albeit not quite identical, compositions. The difference between the two is most notable at higher L, where there is a larger enhancement in the PT population m_{av} than that of the PS.

As with the aforementioned models, the axisymmetric components of m_{av}PS and m_{av}PS were subtracted prior to L-S analysis. Figure 9 shows the real (a and c) and imaginary (b and d) components of the m_{av} models, in the same format as Figure 2. Both sets of functions shown are 4^{th}-order polynomials.

Figure 10 shows the m_{av} model in the equatorial plane using the same format as that in Figure 7, with left panels (a, c and e) showing the m_{av}PS model and the right panels (b, d and f) showing m_{av}PT. Panels a and b is the axisymmetric component, c and d show percentage difference to the axisymmetric component due to the spatial variations, and e and f show the combinations of axisymmetric and periodic components for both models.

The axisymmetric components of both m_{av} models demonstrate that average ion mass peaks at both low L (~2) and larger L ($\geq$ 5) suggesting that the relative concentration of O^+ to H^+ is enhanced in both regions, but with a reduction to $m_{av0} \sim 1$ or 2 amu between $2 \leq L \leq 4$. The variations shown in panels c and d suggest that there is an increase in m_{av} in the morning local time sector for both populations, while there is also a notable decrease in m_{av}PT in the afternoon sector which could be related to plume formation, where plume

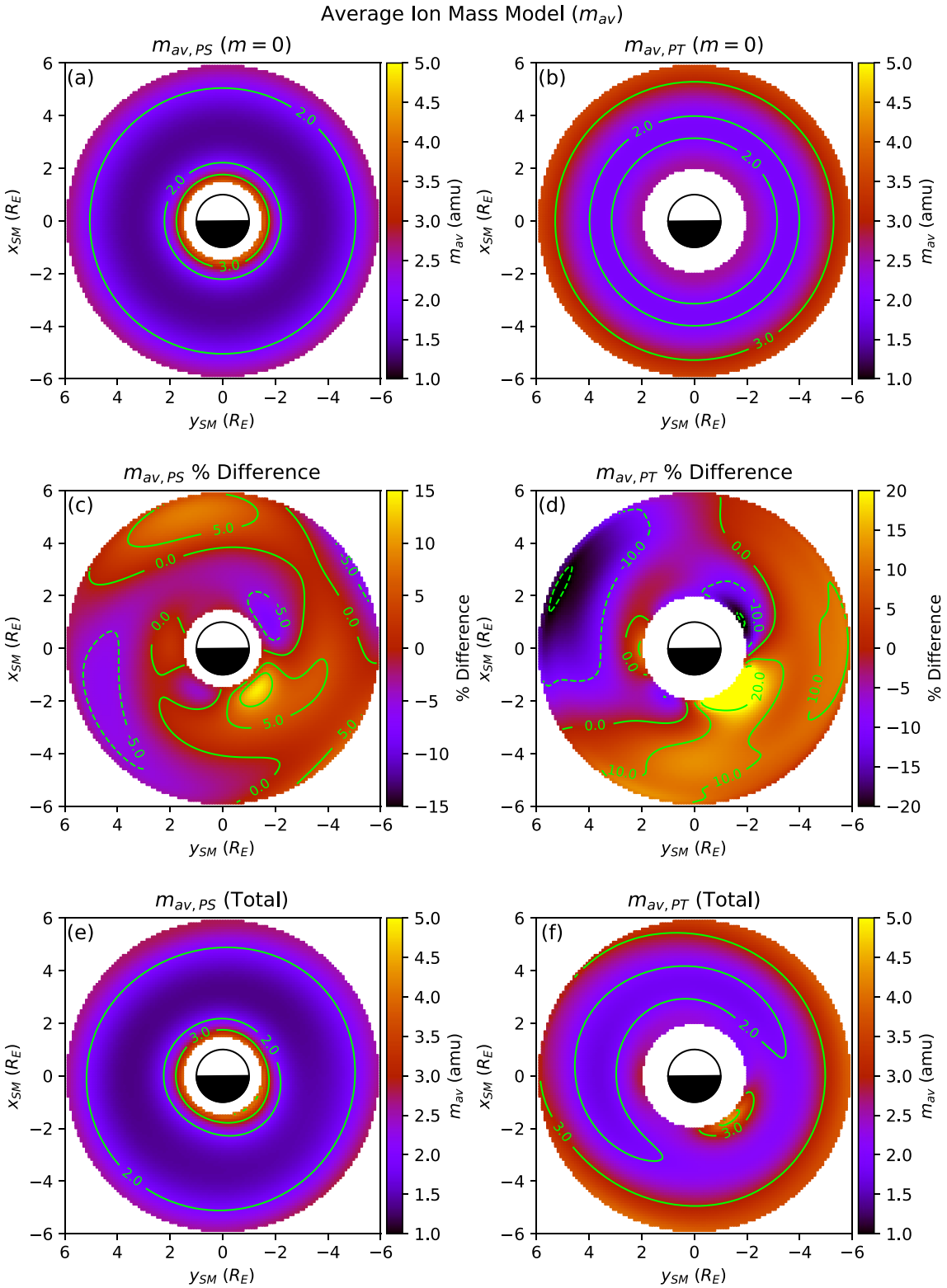

Figure 10. Axisymmetric components (a) and (b), percentage difference to the axisymmetric component due to periodic components (c) and (d) and the combined m_{Av} model (e) and (f) in a similar format to that of Figure 3, where left panels correspond to the plasmaspheric model and right to the plasmatrough model.

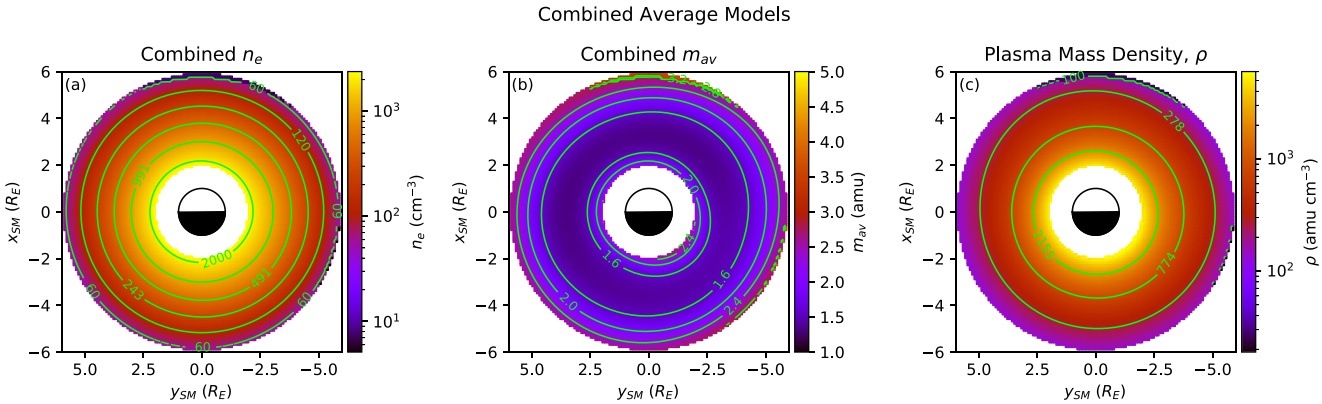

Figure 11. Panel (a) shows the combination of PS density model in Figure 7e and the PT density model in Figure 7f using the probabilities in Figure 3c; the n_ePS model is used in places where $P > 0.5$ and the n_ePT model is used where $P < 0.5$. Panel (b) shows the combination of the m_{av}PS and m_{av}PT models in Figure 10, also using the probability model. Panel c shows the electron density model in panel a combined with the composition from panel (b) to produce a map of plasma mass density, ρ in the magnetic equatorial plane.

plasma typically has lower m_{av} than trough plasma (e.g., Denton et al., 2014). Panels e and f show that the m_{av} distribution in the plasmasphere is largely axisymmetric, whereas the plasmatrough population is less so. The Box-Cox transform of average ion mass means that, even with the periodic variations included, the model does not output unphysical values (i.e., $m_{av} < 1$).

4. Discussion

4.1. Combining the Models

The models produced in Section 3 can be combined to provide an estimate of the most probable electron densities and likely plasma mass densities, ρ, close to the equatorial plane. Figure 11a shows the combination of both PS and PT electron density models from Section 3.2, where the probability model from Section 3.1 is used to decide which n_e model to use. Regions where $P < 0.5$ are most likely to be within the plasmatrough, so the n_ePT model is used; conversely, the n_ePS model is used where $P > 0.5$. Figure 11b shows the combination of the average ion mass models of Section 3.3 using the P model in the same way as in panel a. The probability shown in Figure 3c shows that the majority of the region explored by the Van Allen Probes is usually occupied by the plasmaspheric population, so the densities shown in Figure 11a are mostly PS densities (pink - yellow on the color scale). There is a small sliver of space near $L \approx 5.9$ centered upon noon where $p < 0.5$, this region uses the PT model (black/dark purple).

Figure 11c shows the plasma mass density, ρ, estimated using the electron density calculated for Figure 11a multiplied by the average ion mass in Figure 11b. It is assumed that any contributions to the plasma mass loading by any ion species other than H^+, He^+ and O^+ is negligible and that all ions are singly charged. Plasma mass densities predicted using these model range from ~200 amu cm^{-3} at $L = 5.9$ to ~30,000 amu cm^{-3} at $L = 2$ in the plasmasphere, and are ~35 amu cm^{-3} in the plasmatrough at $R = 5.9$.

Models of total electron density can inform our understanding of key wave processes within the inner magnetosphere. Regions of high density plasma correlate with plasmaspheric hiss (Russell et al., 1969), sharp density gradients are implicated in the chorus to hiss mechanism (Delport et al., 2012), and high density regions on the duskside are important for EMIC wave generation (Usanova et al., 2008). Due to their role in a range of processes, electron density models are also a key input to magnetospheric simulations (e.g., Glauert & Horne, 2005).

The output of these combined models could also act as a useful constraint when using the harmonics of ULF waves observed on the ground (e.g., Wharton et al., 2018) or in space (e.g., Takahashi et al., 2004) to characterize the field-aligned plasma density profile. Depending upon the assumed profile of the plasma (e.g., power law or power law + equatorial enhancement), this model could be used to reduce the number of free parameters to be fitted by providing an estimate of the equatorial density. However, caution should

be exercised when using these average densities-especially at larger L, where the probability model becomes close to 0.5. The inner magnetosphere is a very dynamic region of space and sometimes the average model may assume that a position is occupied by the plasmasphere when, given the current magnetospheric conditions, that position is actually within the plasmatrough (or vice versa), for example, when spatially localized plumes form–these would not be well represented by this model. The models above can therefore be considered to provide two values for ρ: one from the plasmasphere and one from the plasmatrough, where the probability model would provide an idea about which population is more likely to be present.

4.2. Comparison to Other Models

In this section the SPICED model is compared to other models of electron density and composition. Figure 12 shows the comparisons between these models at four different local times: 00:00, 06:00, 12:00 and 18:00. The panels on the left of the figure (a, c, e, and g) show the comparisons of the n_e output from the GCPM (purple dashed), the Sandhu et al. (2016a) model (green dashed), the Sheeley et al. (2001) model (pink dashed) and the Carpenter and Anderson (1992) model (cyan dashed) a with the PS and PT models (yellow and red, respectively) in the region $2 < L < 9.5$. The panels on the right of the figure (b, d, f, and h) show the m_{av}PS (purple) and m_{av}PT (blue) model outputs compared to the average ion mass calculated using the Sandhu et al. (2016b) model (green dashed).

Figure 12 shows that the Sandhu et al. (2016a) model, which combines electron density measurements from the outer plasmasphere, plasmatrough and the near-Earth plasmasheet, provides electron densities which are typically quite close to those of the n_ePT model presented in this paper at $L = 4.5$. The Sandhu et al. (2016a) model was generated using data from $L > 4.5$ which should, for the most part, be made up of plasmatrough measurements; plasmaspheric densities would mostly be excluded from the Sandhu et al. (2016a) study due to the 80 cm^{-3} limit of the WHISPER instrument. The difference between these two models is most noticeable in the midnight and dusk sectors, where the Sandhu et al. (2016a) model predicts enhanced densities. This enhancement may be in part attributed to the possible inclusion of measurements of plasmaspheric electron densities, particularly on the dusk side of the magnetosphere where the plasmasphere typically extends further away from the planet (Carpenter, 1966). The difference between the model presented here and that of Sandhu et al. (2016a) also appears to increase with L, which may be attributed to the fact that the equatorial electron density in the Sandhu et al. (2016a) model is effectively a linear function of L, where other models use non-linear functions to describe this relationship.

The GCPM estimates of electron density at $L > 5$ or 6 are similar in magnitude to the PT model in all local times, but the plasmaspheric portion of the GCPM shows a different trend to the densities output by the PS model presented here. The PS and PT models presented here show that there is typically a difference of around an order of magnitude between the plasmaspheric and plasmatrough densities for $2 < L < 5.9$; the GCPM used a smooth transition between the plasmasphere and plasmatrough, which only exhibits a noticeable step-like change near dawn - otherwise the difference between the two populations appears to only be a change in the gradient with L. This smooth transition between the two populations used by the GCPM model effectively smooths the densities of the two populations together. The advantage of having two separate PS and PT models is that this smoothing across the plasmapause does not happen, allowing for more reliable estimates of n_e in both the plasmatrough and in particular the plasmasphere.

Carpenter and Anderson (1992) and Sheeley et al. (2001) both provide separate models of the plasmasphere and plasmatrough, where each population is described by some non-linear function of L. The Sheeley et al. (2001) models are in very good agreement with the PS and PT models presented in this paper at all MLTs and overlapping L-shells. The Carpenter and Anderson (1992) models exhibit similar plasmasphere and plasmatrough densities, but are only valid for a limited range in local time ($0 \leq \text{MLT} \leq 15$), unlike our models. The plasmaspheric densities provided by Carpenter and Anderson (1992) are generally higher than those predicted here, and the plasmatrough densities are usually lower, where both differences may be explained by the difference in data selection criteria used before creating the models. Carpenter and Anderson (1992) specifically selected plasmaspheric electron density measurements from density profiles along L which were characteristic of a "quiet" plasmasphere, and discarded data along the profile where it either became irregular or exhibited a steeper negative slope with L. The criteria used by Carpenter and Anderson (1992) intentionally excludes lower electron densities which could potentially originate from

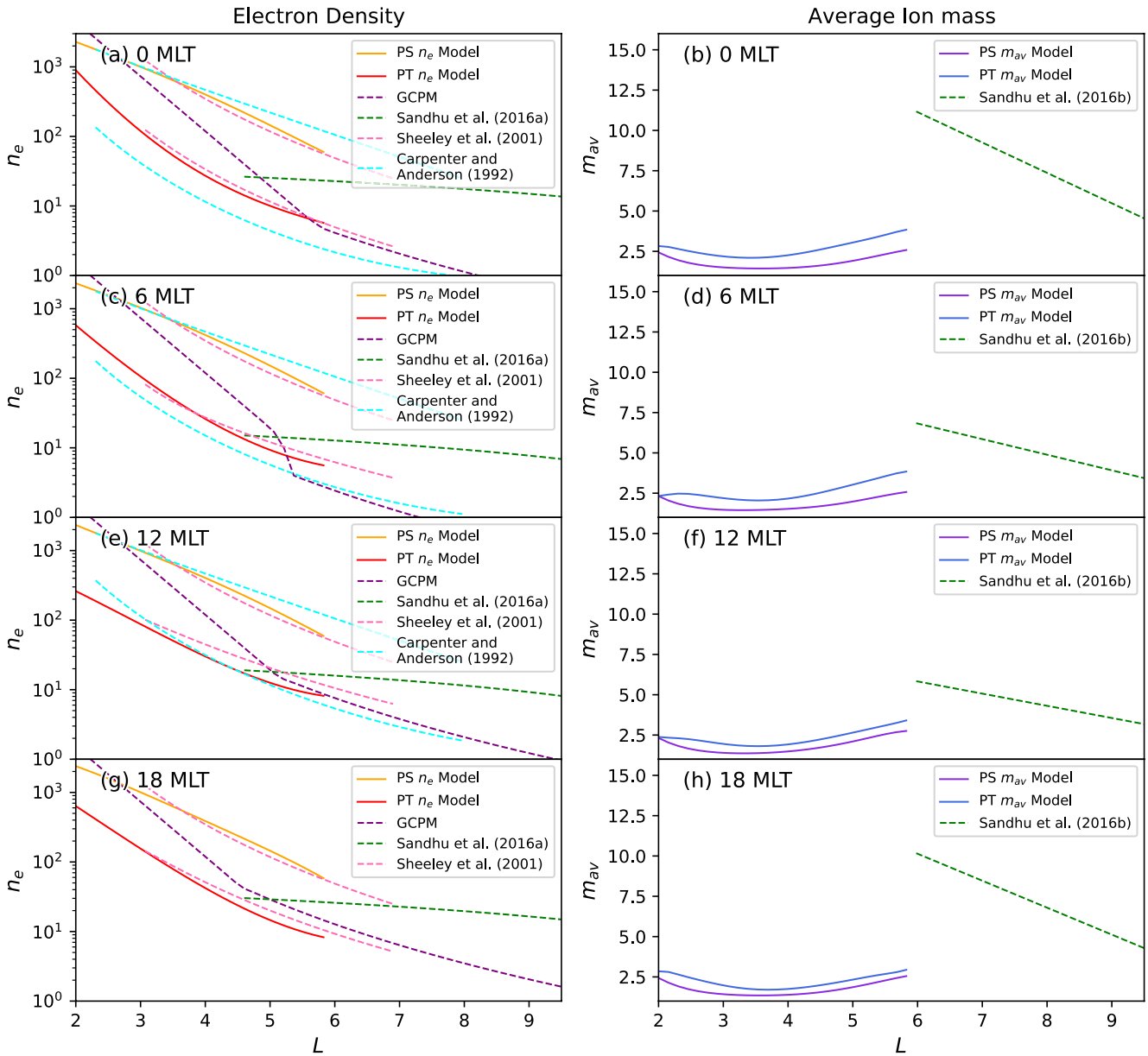

Figure 12. Comparison of average models to previously published models at four different local times. Panels on the left show the comparisons of the PS (yellow) and PT (red) electron density models with the Sandhu et al. (2016a) (green dashed), GCPM (purple dashed), Sheeley et al. (2001) (pink dashed) and Carpenter and Anderson (1992) (cyan dashed) electron density models. Panels on the right show the comparison of the average m_{av} PS (purple) and PT (blue) models with that of Sandhu et al. (2016b) (green dashed).

flux tubes which were still refilling (leaving measurements of the "saturated" plasmasphere), whereas both our model and the Sheeley et al. (2001) model were constructed using all plasmaspheric electron density measurements ($n_e > n_b$, Equation 11). The Carpenter and Anderson (1992) plasmatrough model differs from both the Sheeley et al. (2001) and our plamastrough models for a similar reason–Carpenter and Anderson (1992) selected electron density profiles which were at least a factor of 5 smaller than the "saturated" plasmasphere model in the dayside magnetosphere, and a factor of 10 on the nightside, whereas our model and the Sheeley et al. (2001) model both include electron densities which would have been rejected by Carpenter and Anderson (1992). With the inclusion of our P model, our set of models has an advantage over those of Carpenter and Anderson (1992) and Sheeley et al. (2001) in that it provides an estimate of which populations are most likely at different L-shells and MLTs. Our average models are also improved upon in Section 4.3, where they are all parameterized based on geomagnetic conditions.

The right hand panels of Figure 12 show that, at the interface where the m_{av} models presented in Section 3.3 and the Sandhu et al. (2016a) model meet ($L = 5.9$), there can be substantial differences in the predicted average ion mass. A possible explanation for the difference is that the HOPE instrument is capable of detecting particles with lower energies than that of CODIF and may therefore provide different relative concentrations of the ions. Another possible reason for the different ion concentrations is that the datasets used to create each model originate from times associated with different levels of solar activity; the data set used by Sandhu et al. (2016a) spans the years 2001–2005 where the median SMR index is ~-8 nT, whereas the median SMR index for this study was ~-2 nT, where a more negative SMR index corresponds with higher m_{av} (this is discussed further in Section 4.3). A third possible explanation of the difference in m_{av} is that the measurements used to create this model originate primarily from close to the magnetic equator ($R_{norm} \geq 0.95$), however those that were used to create the Sandhu et al. (2016a) model are from further along the field lines ($0.5 \leq R_{norm} < 0.9$, or magnetic latitude $18 < |\theta| < 45°$ assuming a dipolar field) meaning that the equatorial m_{av0} produced by that model is obtained by extrapolation. The data set used by Sandhu et al. (2016b) may also have been contaminated by plasmasheet material as the model extends to large L-shells.

The average ion mass models created here can also be compared with magnetoseismological studies which have use ULF waves to determine m_{av}. One such example is provided by Takahashi et al. (2006), where m_{av} is predicted to be typically from ~2–4 amu in the region $\sim 4 < L < 8$ (see Figure 7b of Takahashi et al. (2006)). Another study by Takahashi et al. (2008) also used ULF wave activity to determine average ion mass for a pass through the plasmatrough and plume and found that m_{av} ranged from 4–16 amu in the plasmatrough and ~1 in the plume. Similarly, during two events (one quiet time, on active) Denton et al. (2014) estimated values for m_{av} of up to 10 amu in the plasmatrough and close to unity in the plume.

The GCPM estimate for m_{av} (not shown) is substantially lower than both the model presented here and that of Sandhu et al. (2016a). The reason for this is that the GCPM assumes a constant 1% relative concentration of oxygen ions to protons in the plasmasphere, leaving any changes in m_{av} calculated by the model solely due to changes in the relative concentration of helium ions to protons. The data presented in Figure 8 suggest that oxygen makes a significant contribution to the plasma mass loading of field lines at low L-shells, which GCPM does not predict.

4.3. Model Parameterization Using Artificial Neural Networks

The aforementioned models show an average picture of the density and composition of the Earth's near-equatorial inner magnetosphere; this set of models can be used to provide an example of the most probable characteristics of the PS and PT plasma populations, but there is no information on how these plasmas may vary. The Earth's magnetosphere is by no means a steady system, variations in Solar and geomagnetic activity drive large changes in the morphology and composition of both the plasmasphere and plasmatrough, therefore it is prudent to attempt to determine how this model may vary under different levels of activity. In this section, we briefly describe the implementation of n_ePS, n_ePT, P, m_{av}PS and m_{av}PT models which can be scaled based on changes in geomagnetic activity.

The first step in scaling these models was to determine what parameter(s) would be most suited to each one. For simplicity, a single extra parameter, z, was chosen for each of the five models. Appendix B describes in detail the process by which the parameters were selected. Conveniently, the best parameter for scaling all 5 models is the SMR index (Newell & Gjerloev, 2012), which is a measure of the horizontal deviation in the Earth's surface magnetic field due to variations in the ring current; this index is similar to the *Dst* and SYM-H indices. The magnitudes of number density and heavy ion concentrations, as well as the size and shape of the plasmasphere, is known to respond strongly to ring current indices (Goldstein et al., 2019; Kronberg et al., 2014; Sandhu et al., 2017; Wharton et al., 2020). During storm times, heightened convection and field-aligned currents result in strong convective erosion and enhanced heavy ion outflows.

With the additional parameter, z, the functions $F_0(L)$, $R_m(L)$ and $I_m(L)$ from Equation 8 were modified to become $F_0(L,z)$, $R_m(L,z)$ and $I_m(L,z)$, each of which is a non-linear 2D function. Artificial neural networks (ANNs) were trained to act as these functions because they are particularly well suited to solving highly non-linear problems and have been proven to be capable of creating similar models (e.g., Chu et al., 2017; Zhelavskaya et al., 2017).

In order to create training data for each of the ANNs, the Lomb-Scargle analysis used to create the average models was performed on small subsets of the data. Each subset contains 5% of the total data, which covers a small range of SMR; a total of 951 subsets are used starting from the lowest 5% of SMR, to the highest 5% in steps of 0.1%. The SMR range covered by the median values of the parameters bins was −41 to +16 nT. These parameter ranges were extended by splitting the most extreme data bins into smaller bins, each containing 1% of the total data, resulting in a total of 991 subsets. This extended the SMR ranges to −75 to 27 nT and gives the model the ability to provide density and composition predictions for a wider range of magnetospheric activity levels. Every subset provides F_0, R_m and I_m for up to 381 values of L, providing a total of up to ~377k samples.

The implementation of the ANNs used here is addressed specifically in Appendix C which describes how the network architectures were chosen and how they were trained. As with the average model, the parameters and the code for the scaled models are all available in the Supporting Information S1 and at https://github.com/mattkjames7/spicedmodel.

4.4. Comparison to Real Data and Other Scalable Models

In this section the models are compared to real data, where the primary focus is upon the parameterized variant of the models using the trained ANNs described in the previous section.

Figure 13 shows the comparison between electron density data (top panels a and b) with the combined output of the n_ePS, n_ePT and P models (bottom panels c and d), using the same method as described for Figure 11a. Panel e shows the probability density function of the SMR index for the entire data set, where the lowest and highest 5% of SMR measurements have been highlighted in green. Panel a shows the electron densities measured near to the magnetic equatorial plane for the 5% of data collected during times with the lowest SMR, in the range −249 to −30 nT with a median of −41 nT. Panel c shows the corresponding combined electron density model output using the median value of SMR from panel a. Both the data and the model show that during low values of SMR, the plasmapause moves significantly planetward in all local times except near to dusk where a plume forms. The right panels (b and d) of Figure 13 show the equivalent to the left panels using the 5% of data associated with the highest SMR. Both panels b and d show that the region from $2 < L < 5.9$ is predominantly occupied by a large plasmasphere during periods of high SMR, with the plasmapause location beyond the scope of the model in all local times. Any mismatch of shape of the plasmapause in panel c with that of panel a could be attributed to there being relatively little data to train the model near the more extreme values of SMR; as panel e shows, 90% of the data (949 out of 991 SMR bins from section Appendix B) originate from times when $-30 < SMR < 13$ nT, a range which is only ~20% of the size of the range in panels a and c, so the model is likely to be somewhat biased towards times with more commonly observed values of SMR.

Figure 14 shows a comparison of the measured and modeled m_{av} in the same format as that of Figure 13 with the same SMR bins. In the low SMR case (panels a and c), both plasmatrough and plasmasphere exhibit generally higher m_{av} values than those predicted by the average models implying more O^+ ions populating the inner magnetosphere during disturbed times, with the plasmatrough also displaying more significant local time variations. Panels b and d show the high SMR case, where the plasmasphere occupies the entire model L range, as in Figure 13d. During high SMR, the m_{av}PS model predicts overall that the average ion mass is less than both the low SMR example and the average model-particularly at larger L. Unlike the electron density model, where there is approximately an order of magnitude step between the two plasma populations, the change in average ion mass over the predicted plasmapause is much less severe (typically ~ 1 amu or less), which suggests that any change in the local Alfvén speed across the plasmapause boundary will mostly be attributed to changes in the overall plasma density, rather than the composition. The increase in m_{av} at high L in the low SMR case is consistent with the recent observations of the oxygen torus made by Nosé et al. (2018) using Arase (Miyoshi et al., 2017) and Van Allen Probe data. The observations of Nosé et al. (2018) suggested that the oxygen torus was localized in MLT, with an enhancement observed near dawn ($m_{av} = 3.5$ near $L \sim 5$ – similar to that predicted here), but no notable enhancement at dusk. While the true azimuthal extent of the oxygen torus observed by Nosé et al. (2018) is unclear, it did suggest that the generation mechanism proposed by Roberts et al. (1987) may be in play.

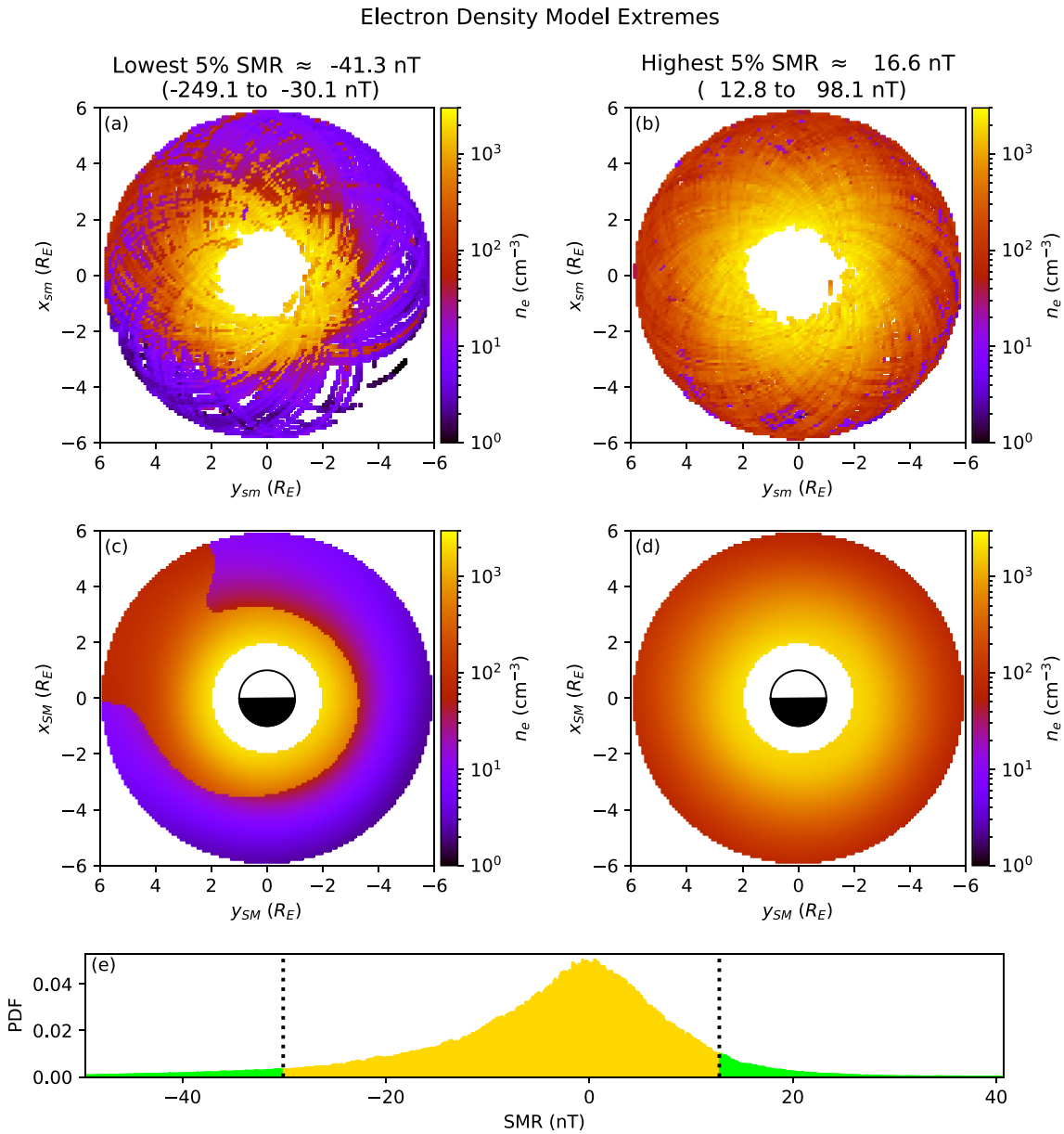

Figure 13. Measured electron densities (a) and (b) and combined PS/PT model outputs (c) and (d) for the lowest values of SuperMAG ring current index (SMR) (left panels) and highest values of SMR (right panels). Panel e shows the probability density function for SMR, where the green shaded regions correspond to the lowest and highest 5% of SMR indices (a small number of SMR measurements extend to ~ −250 nT, beyond the limits of the plot).

The comparisons made between the model output and the data in Figures 13 and 14 show that the parameterized models provide a reasonable representation of the data in the specific cases where the SMR index has deviated significantly away from normal values, whereas Figure 15 shows a more general comparison. In Figure 15 both the average and the parameterized versions of the models are compared directly to the data. Each panel shows a 2D histogram of the original data on the *x*-axis and the model output on the *y*-axis, where a green dashed line represents the identity line where data and model output would be equal. The root mean square (RMS) differences and mean absolute errors (MAE) for each parameter are shown in the bottom right of each panel, where the MAE and RMS values for the density plots are calculated using the Box-Cox transformed densities. The top panels (a, b, c and d) compare the data with the predictions made using the average models constructed in Section 3, while the bottom panels (e, f, g and h) show the equivalent comparisons made using the parameterized models constructed in Section 4.3.

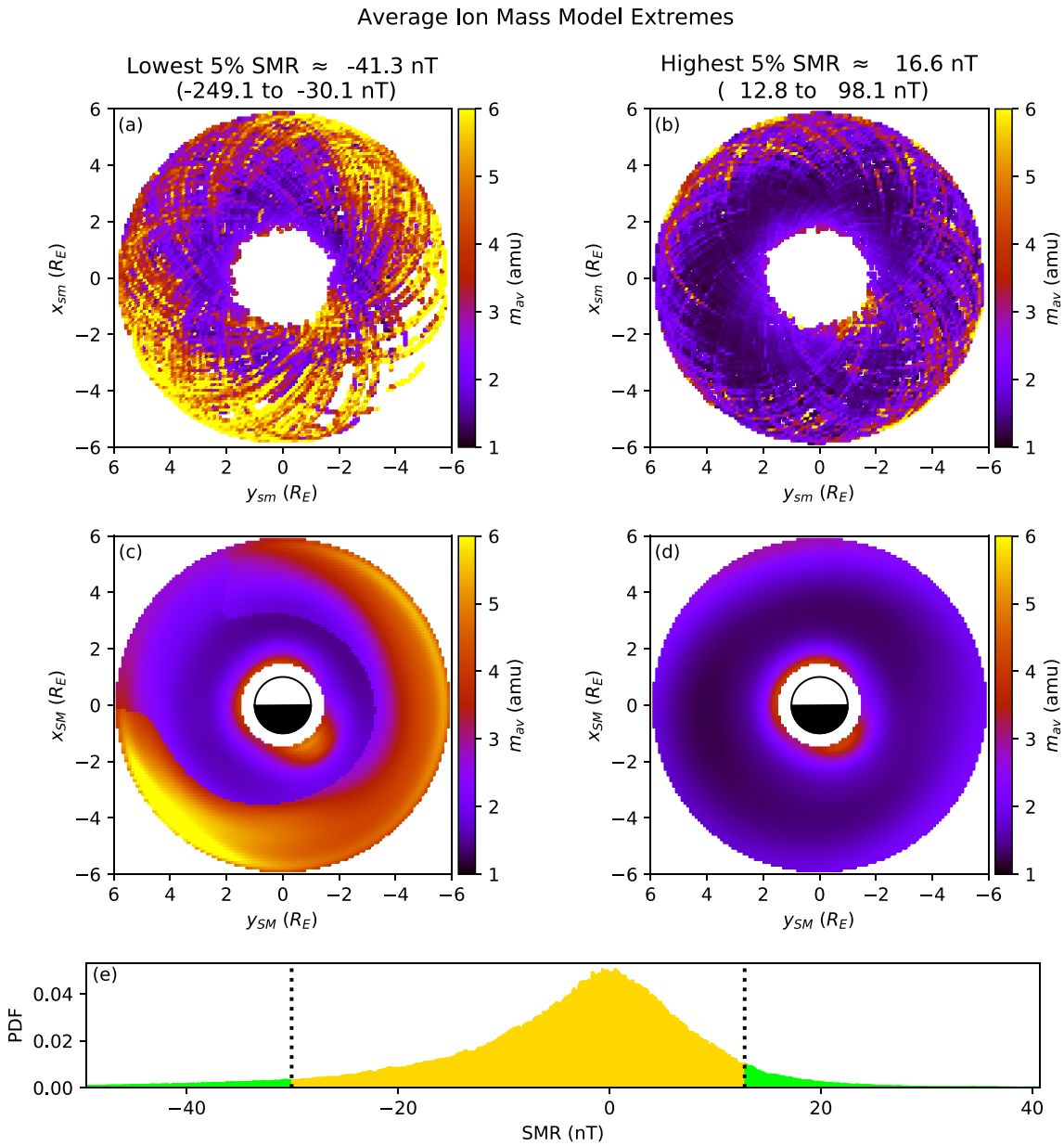

Figure 14. In the same format as that of Figure 13, measured average ion mass (a) and (b) and m_v model outputs (c) and (d) for the lowest values of SMR (left panels) and highest values of SMR flux (right panels).

Panels a and e of Figure 15 show that, in both PS models, the plasmaspheric electron density are generally in agreement with each other, but the MAE and RMS errors are smaller in the parameterized version of the model. In panels b and f, the model plasmatrough densities are visibly closer to the data, however both plots show a small population which lies away from the identity line. This population of outlier electron densities appear to be a factor of ~ 4 larger than expected, so are potentially either misclassified plasmaspheric measurements, or measurements made while crossing the plasmapause.

Panels c, d, g, and h show the m_{av} comparisons using the same format as the electron density plots, where c and d present the comparisons between average PS and PT models, respectively and g and h show their scaled equivalents. In these plots, it is apparent that most of the m_{av} distribution is concentrated between 1 and 2 amu, rather than being spread across several orders of magnitude like n_e. In all four of the m_{av} comparisons, the models typically predict similar values to those observed - but there are some outliers. In panel c,

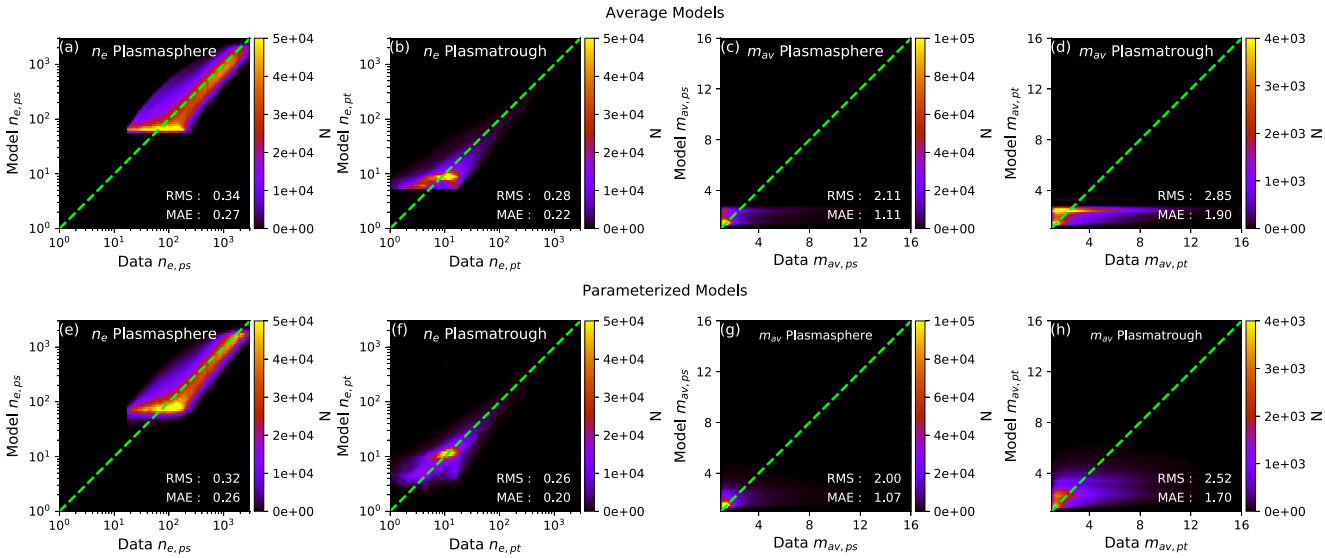

Figure 15. Comparison average models panels (a–d) and parameterized models panels (e–h) with data from the Van Allen Probes. Panels (a) and (e) show the comparisons with plasmaspheric n_e data; in (b) and (f) the plasmatrough n_e; (c)and (g) show the plasmaspheric m_{av}; and panels (d) and (h) show plasmatrough m_{av}. In all panels, the green dashed line shows the identity line where data and model are equal and the color scale represents the number of model/data points in each bin.

there is a relatively small outlier population which is consistently over-estimated by the average m_{av}PS model, where the scaled version of the model (panel g) manages to successfully reduce the number of outliers. The comparison of the data with the average m_{av}PT model in Figure 14d shows a population which is not easily reproduced by the model–the model typically predicts $m_{av} \sim 2.5$ amu for measurements which are spread from ~ 1 to > 10 amu. While the scaled model (panel h) improves the m_{av}PT predictions, there is still a large amount of spread away from the identity line. Proportionally, most of the outlier population in panel d exists at $L > 4$, where the average ion mass is highly variable in the plasmatrough (e.g., see Figures 17e and 17f later in this section).

Comparisons of the electron density models from Section 4.3 with the PINE model (Zhelavskaya et al., 2017) and the Sandhu et al. (2017) model are presented in Figure 16. The format is similar to that of Figure 12 except that both sides show electron densities: the left panels (a, c, e, and g) show the models in normal conditions where SMR ≈ 0 nT, the right panels (b, d, f, and h) show the models at times where SMR ≈ -75 nT. In all panels, the Sandhu et al. (2017) model is shown in green; the PINE model in black; the PS and PT models are represented by orange and red lines, respectively; and the solid gold line shows the most probable electron density as calculated in Section 4.1 by combining the PS, PT and *P* models. As we do not have access to the PINE model, only a limited number of model outputs available in the PINE repository (ftp://rbm.epss.ucla.edu/ftpdisk1/PINE), we selected three model images which corresponded with times when the SMR matched the values used in Figure 16.

In the left panels, the PINE model output is taken from September 23, 2013 at 03:30 UT, when SMR had remained close to 0 for ≈2.5 days. This model is largely in agreement with our combined n_e model for *L*-shells up to ~ 4.5, where both predict densities characteristic of the plasmasphere. At larger *L*-shells, particularly at noon and dawn, the PINE model starts to gradually deviate away from plasmaspheric densities, towards those which resemble the plasmatrough. This is in contrast to the SPICED model which predicts that the plasmasphere is the most likely population to exist for the entire range of *L* at SMR = 0 nT. The PINE model images compared in the right panels of Figure 16 both originate from times when SMR was close to −75 nT (dashed and dotted black lines). The dashed line represents the PINE model output shortly after the onset a geomagnetic storm, during the main phase (at 03:30 UT on June 6, 2013) and the dotted line represents the output during the start of the recovery phase of the storm (at 14:00 UT on June 6, 2013). In both storm-time cases, the PINE model is mostly in agreement with the models presented here, where the plasmasphere was eroded significantly-particularly from midnight through to noon. The largest difference is near noon,

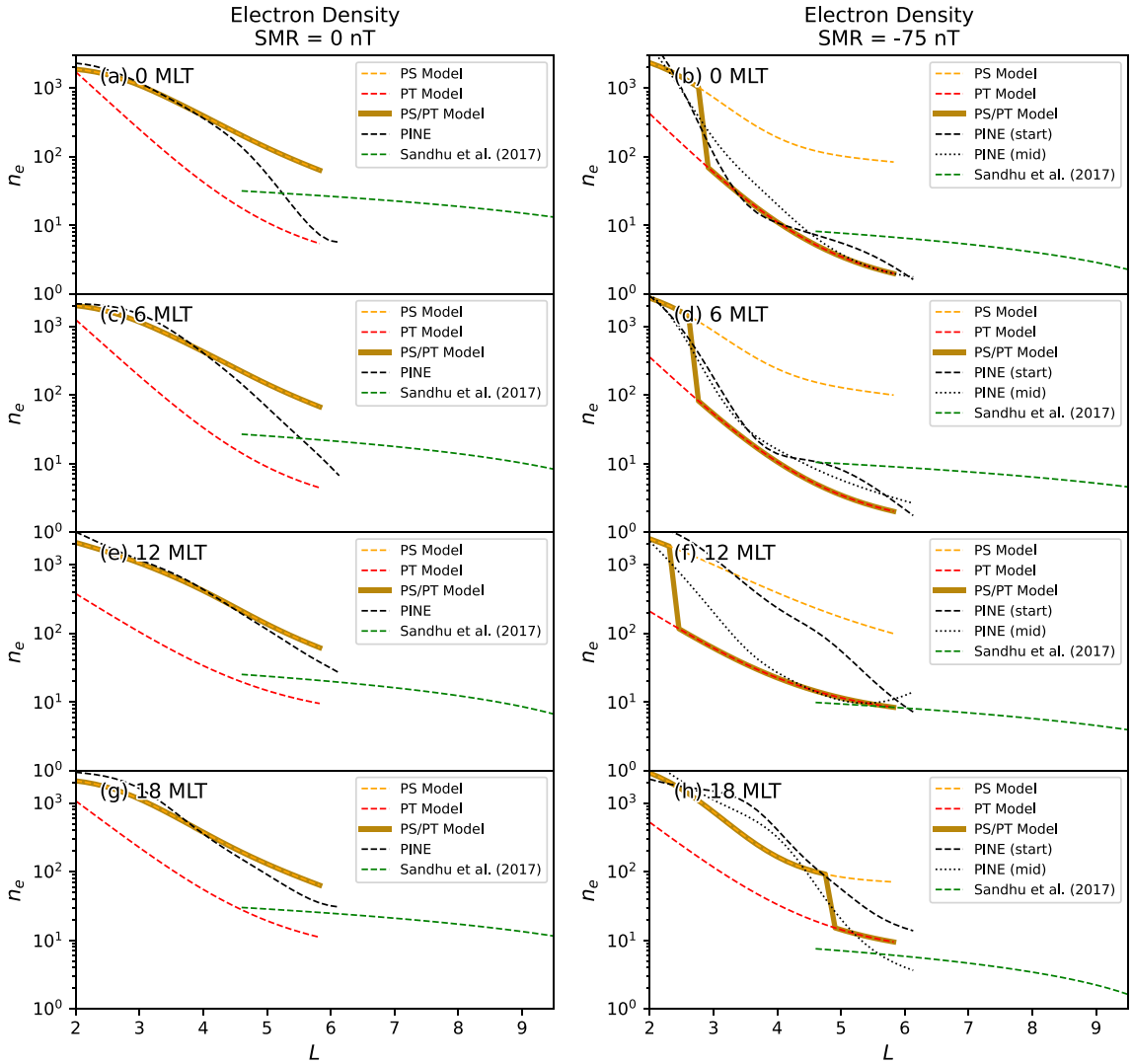

Figure 16. Comparison of the scaled PS and PT models to previously published models at four different local times and two different levels of SMR. The panels on the left correspond to the average state of the ring current where SMR = 0 nT, panels on the right show the model densities when SMR ≈ -75 nT. All panels show the comparisons of the PS (yellow dashed) and PT (red dashed) electron density models with the scalable Sandhu et al. (2017) (green dashed) and PINE (black dashed). The solid gold line represents the most probable electron density estimated by combining the PS, PT and *P* models.

where the plasmasphere is predicted to extend to much larger *L*-shells early during the main phase of the storm; later in the storm, during the recovery phase, the plasmapause is at a much lower *L*-shell, and both models are in closer agreement. The PINE model has the advantage over the model presented here that it is capable of taking into account the time history of geomagnetic parameters; the downside of the PINE model is that there is always a very smooth change in the electron densities across the plasmapause because both plasmasphere and plasmatrough populations are modeled together. Modeling the PS and PT separately, and combining these models with the *P* model, allows for better predictions of n_e closer to the plasmapause, rather than effectively smoothing the densities of the two populations together like the PINE model. Gradients in density around the plasmapause can vary from being very gradual and not very well defined during times when the plasmasphere is refilling; it can also be very sharp during periods of erosion (Chappell, 1972).

The comparison with the Sandhu et al. (2017) electron density model in Figure 16 suggests that the electron densities it predicted at $L \sim 4.5$ are similar to those of the PT model at most local times, during both normal and storm-time. The Sandhu et al. (2017) model is scaled using the *Dst* index, which has been shown to

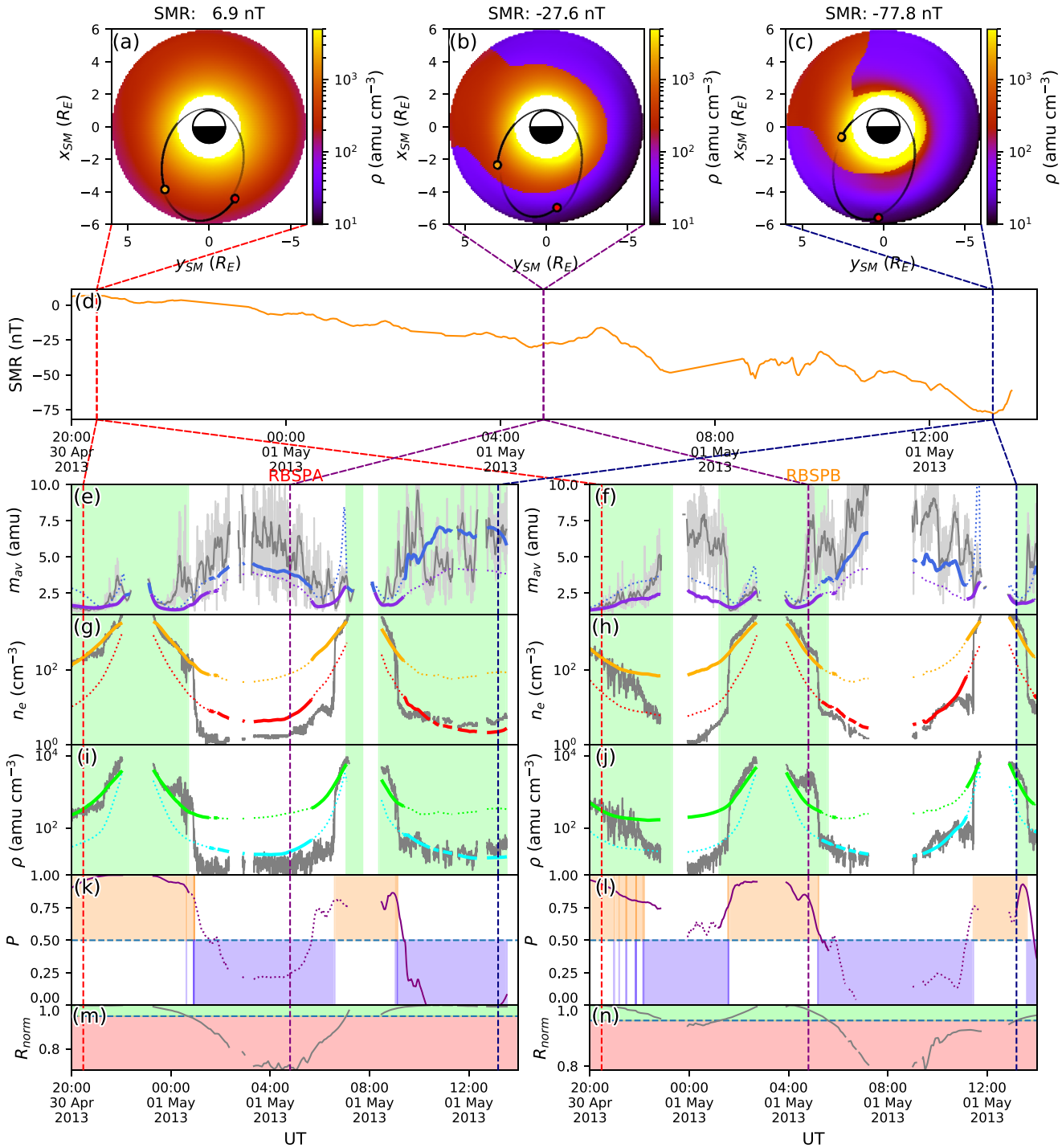

Figure 17.

approximately match SMR (Bergin et al., 2020), so for the purpose of the comparison made here–SMR is used in place of *Dst*. Both models suggest that the plasmatrough electron densities drop during low SMR compared to higher SMR, albeit by different amounts. As with the average models presented in Figure 12, the difference between the two models increases with L due to the Sandhu et al. (2017) model effectively varying linearly with L.

Figure 17 shows an example of the model being used to describe the state of the equatorial inner magnetosphere during the main phase of a geomagnetic storm by driving the model using time-series SMR indices, while showing direct comparisons to Van Allen Probe data. The top three panels a, b and c, each show the plasma mass density in the equatorial plane as predicted by the combined models at three different times during the main phase of the storm. In each panel a–c, the positions of probes A and B are represented by red and orange circles, respectively; in each case, the orbits were oriented such that apogee was around 23 MLT. Panel d shows the SMR indices from 20:00 on April 29th to 14:00 on May 1st 2013. The red, purple and blue vertical dashed lines in panel d and all subsequent panels, represent the times which correspond to the model plots in panels a, b and c, respectively. Below panel d, data from each spacecraft are shown, where probe A data are on the left and probe B data on the right. In panels e to j data from the spacecraft are in gray, while the model outputs are in color; both model outputs (from PS and PT) are presented in each panel as dotted lines, which become solid depending on which population the P model predicts the spacecraft to be within. Panels e and f show m_{av} measured by the Van Allen Probes in gray and modeled in blue (PT) and purple (PS). Panels g and h show the electron densities, where the PS and PT models are both presented in yellow and red, respectively. Panels i and j show the plasma mass density for the PS (green) and PT (cyan), calculated using the m_{av} and n_e data and models from the panels directly above. The P model output for each probe is presented in panels k and l as a purple line, where $P >= 0.5$ represents times when the probes are likely to be within the plasmasphere. The shaded areas represent the PS (orange) and PT (purple) classifications based on the measured electron densities. Finally, panels m and n show the value of R_{norm} for each spacecraft, where the green shaded area represents the valid range of $R_{norm} >= 0.95$ – the times when this condition is met are shown in panels e–j by a green shaded background. An animated version of this plot is included in the Movie S1 for this paper.

During the time shown in Figure 17d, the SMR index drops from just above 0 to around −75 nT, reaching the lower SMR limit of the models, beyond which the model is not likely to be capable of providing reliable predictions. At the start of the event, the plasmasphere extends to beyond the outer boundary of the model. As time progresses and SMR drops, panels b and c show that the plasmasphere is predicted to shrink and form a plume near dusk. The majority of the changes to the modeled plasma mass density observed in Figures 17a–17c are driven by the variation in SMR shrinking the plasmasphere compared to the changes in composition.

The data shown in panels e and f of Figure 17 show that the m_{av} measurements can be fairly noisy (particularly in the plasmatrough), but are mostly in some agreement with the model when within the valid R_{norm} range. Both n_ePS (upper yellow line) and n_ePT (lower red line) models provide reasonable estimates of the plasmaspheric and plasmatrough densities when compared to the data. The PS model appears to perform somewhat better than the PT model, this is likely to be because 75% of the collected electron densities originated from the plasmasphere, whereas the plasmatrough does not usually extend to lower L-shells. This resulted in less plasmatrough data to train with in this region of space. A similar story is true for the ρ model comparison presented in panels i and j, where plasmaspheric mass densities are generally predicted better than plasmatrough ones. Panels k and l show that the model provides reasonable estimates of when the probes cross the plasmapause from one population to the other even when outside of the valid R_{norm} range. The P model is not perfect though, as panel l shows that probe B traversed the plasmatrough in the hours surrounding midnight, but the model still predicted P slightly higher than the threshold required to switch from PS to PT densities.

Figure 17. Model output during the main phase of a geomagnetic storm starting around 00:00 1st May 2013. Panels (a), (b) and (c) show equatorial projections of the plasma mass density calculated using the parameterized models (same format as that using in Figure 11c) where panel a shows the state of the model prior to the storm at ≈20:30 UT, 31st April; and panels (b) and (c) show the model at the times 4:50 and 13:10 UT on May 1st, respectively. Each of panels (a–c) show the positions of probes A (red circle) and B (orange circle) at the time. Panel (d) shows the value of SMR during the event, where the red, purple and blue vertical lines represent the times corresponding to panels (a), (b) and (c), respectively (also visible in all subsequent panels). The remaining panels (e–n) show time series data and model outputs for both probes, where panels on the left correspond to probe A and those on the right are for probe B Panels (e) and (f) show the average ion mass measured by each probe smoothed using a 5 min sliding window in gray (original data in light gray) with both PS (purple) and PT (blue) model outputs; solid lines show the model output for the most probable plasma population according to the probability model. Panels (g) and (h) show the electron densities (gray), with the PS model output (orange line on top) and the PT model output (red model below). Panels (i) and (j) show the plasma mass density as measured (gray) and modeled (cyan/green). Panels (k) and (l) show the probability model output (purple line) and whether the probes are in the PS (orange shading) or PT (purple shading). Using the probability from panels (k) and (l), the solid portions of the model lines in panels (e–j) represent the most probable model output. Panels m and n show the R_{norm} of the spacecraft, which is within the model range when $R_{norm} \geq 0.95$ (green shaded region).

The scalable models presented in this paper are all parameterized using a single instantaneous value of SMR. This simple parameterization means that times corresponding to identical SMR values during different phases of a storm, such as that presented in Figure 17, would incorrectly generate the same model. The models could be improved by using a weighted history of SMR, similar to the weighted K_p used by Gallagher et al. (1988), or by creating models for specific phases of a storm. A potentially better way of improving the SPICED model would be to include a history of multiple driving parameters as inputs, similar to the method used by (Zhelavskaya et al., 2017), where a 96 h history of multiple parameters is used to drive the model. Such developments will be included in future iterations of SPICED.

5. Conclusion

In this paper, measurements of electron density and ion composition made by the Van Allen Probes are used to create models of the equatorial inner magnetosphere. The first set of models are created in Section 3 are used to describe the average state of this region. Two models of average ion mass are created using the relative concentrations of hydrogen, helium and oxygen ions–one for the plasmasphere and one for the plasmatrough. Two models of electron densities are created, one describing plasmaspheric electron densities, the other describing the plasmatrough population. A fifth model is created to describe the probability of a position on the magnetic equatorial plane being within the plasmasphere or not and is used in conjunction with the average ion mass and two electron density models to provide an estimate of the average plasma mass density near the equatorial plane.

The average models described above are then parameterized such that they can be used to describe the ion composition, electron density and probable plasmasphere shape during varying geomagnetic conditions by utilizing artificial neural networks. The models are shown to provide a good representation of the data overall, especially at times when the SMR index remains within a normal range. Both sets of average and scalable models compare well with previously published models, also providing improvements in n_e predictions where other models may be mixing the plasmasphere and plasmatrough densities. These models are also the only set of models which are capable of providing both electron density and average ion mass predictions within the region $2 \leq L \leq 5.9$ – similar to the way that the Sandhu et al. (2016b); Sandhu et al. (2016a, 2017) models do for the region $5.9 \leq L \leq 9.5$.

The predictions made by these models can be used to aid the study of ULF wave propagation within the vicinity of the Van Allen Probes. By providing the electron density and average ion mass, the models can be used to provide estimates of the equatorial plasma mass density and, with additional magnetic field data, determine an approximate prediction of the Alfvén speed in the region for a range of geomagnetic conditions.

Future work in this area could include extending this set of equatorial plasma models using data from other spacecraft at higher L-shells. The models could also be extended using data from spacecraft with higher orbital inclinations (e.g., Arase) to be able to determine the field-aligned profile of m_{av} and n_e as done in Sandhu et al. (2016b) and Sandhu et al. (2016a). Ground-based and in-situ ULF wave observations would also have the potential to extend the model further along the field lines by using the harmonics of the waves to determine the field-aligned structure of the plasma.

Appendix A: HOPE Moments

This section describes the derivation of cold ion densities from HOPE level 3 omni-directional spectra by integrating the differential energy flux and correcting the oxygen ion densities.

Following the work of Genestreti et al. (2017), the HOPE energy bins, E_j, are related to the ambient plasma energy, E_j' by $E_j' = E_j + e\phi_{sc}$, where ϕ_{sc} is the spacecraft potential as measured by the Electric Field and Waves instrument (EFW), (Wygant et al., 2013). The spectra are then integrated from E_{min}' (the minimum energy limit of the HOPE instrument) to 20 eV using a Reimannian discrete sum (e.g., Genestreti et al., 2017; Goldstein et al., 2014) in order to obtain an initial partial energy number density (PEND),

$$n_i \approx 4\pi\sqrt{\frac{m_i}{2}}\sum_j E_j^{'\frac{1}{2}}\left(\frac{\Delta E_j}{E_j}\right)J_{ij}, \tag{A1}$$

where m_i is the mass of ion species (H^+, He^+ or O^+) and J_{ij} is the differential energy flux measured by energy bin number j.

The densities calculated using Equation A1 were then used to determine the fractional ion concentration for each species,

$$f_i = \frac{n_i}{\sum_i n_i}. \tag{A2}$$

Unlike for cold proton and helium ions, the cold oxygen ion concentration, f_{O+}, has been shown to exhibit a dependence with temperature ($f_{O+} = 10^{-2.48}T^{1.13}$, Goldstein et al. (2019)), so spectra provided by HOPE must be extrapolated in order to obtain better estimates of the oxygen density. The oxygen densities are corrected by using the method developed by Goldstein et al. (2019).

A summary of the method used by Goldstein et al. (2019) is as follows: the first step was to determine the local bulk plasma velocity in the rest frame of the spacecraft, $v_{bulk} = \left|v_{sc} - v_{E\times B}\right|$, where v_{sc} is the spacecraft velocity and $v_{E\times B}$ is velocity of the local $E \times B$ drift calculated using the Volland-Stern electric field model (Stern, 1975; Volland, 1973) with the subauroral polarization stream (Goldstein et al., 2005). The bulk energy, $E_{bulk} = \frac{1}{2}m_i v_{bulk}^2$ was then used to determine which method by which the upper limit of the oxygen temperature, T_{O+} would be calculated. If $E_{min} > 1.25E_{bulk}$, the PEND technique (Genestreti et al., 2017) is used to calculate temperature; otherwise it is determined by numerically integrating the spectra to obtain pressure, p_{O+} and density, n_{O+} where

$$T_{O+} = \frac{1}{k_B}\frac{p_{O+}}{n_{O+}}. \tag{A3}$$

The lower limit of the oxygen temperature was then estimated to be $T_{O+}^{'} = 0.27T_{O+}$.

The upper and lower limits of oxygen temperature were subsequently used to adjust the fractional ion concentration of oxygen such that $f_{O+}^{'} = (T_{O+}^{'} / T_{O+})^{1.1} f_{O+}$ or, equivalently: $f_{O+}^{'} = 0.27^{1.1} f_{O+} \approx \frac{f_{O+}}{4}$.

Then, using the adjusted fractional ion concentration, a new set of ion densities were calculated,

$$n_i^{'} = \frac{f_i^{'}}{\sum_i f_i^{'}} n_e, \tag{A4}$$

where n_e is the electron density provided by EMFISIS.

The two sets of densities, n_i and $n_i^{'}$, were both used to calculate lower and upper limits to m_{av}, respectively, using Equation 6. The mean of the upper and lower limits to m_{av} was then used to generate the models.

Appendix B: Feature Analysis

This section compares a number of different indices pertaining to Solar and geomagnetic activity in order to establish which parameters may be best suited to scaling each of the four models introduced in Section 3.

The input parameters to an ANN are called "features," where each feature corresponds to an input node to the network. The purpose of the ANNs would be to map the input features to a set of output model parameters: F_0, R_m and I_m. An obvious feature to include for all models is L, because all three model parameters are functions of the L-shell (see Equation 8). This section determines which feature would be best to use alongside L as a second feature, which would correlate the most with the largest variations in the model parameters.

The potential features tested here include the F10.7 index, Kp-index (Bartels et al., 1939), OMNI parameters (King & Papitashvili, 2005) (including magnetic field orientation, solar wind velocity, Mach numbers etc.) and SuperMAG geomagnetic indices (Newell & Gjerloev, 2011, 2012)–see Table B1. Prior to feature analysis, all parameters were scaled such that they vary over similar scales, either such that their ranges were

limited to the range −1 to +1, or such that their means were equal to 0 and standard deviations equal to 1. In some cases, where parameters varied over a large range and exhibited a non-Gaussian distribution, the Box-Cox transformation (see Equation 14) was used and then data were normalized to have a mean of 0 and a standard deviation of 1.

Table B1
Table Showing the Parameters Included in the Feature Analysis, the First Column Lists the Parameters, the Middle Column States the Source of Each Parameter and the Final Column Describes Each Parameter Briefly

Parameter	Source	Description
n_e	EMFISIS	Electron density
L	T96 Trace	L shell
MLT	T96 Trace	Magnetic local time
Dipole Tilt	T96 model code	Dipole tilt angle
SMR	SuperMAG	Ring current index, similar to SymH and D_{st}
SMR00	SuperMAG	Local time ring current index (21–03 MLT)
SMR06	SuperMAG	Local time ring current index (03–09 MLT)
SMR12	SuperMAG	Local time ring current index (09–15 MLT)
SMR18	SuperMAG	Local time ring current index (15–21 MLT)
SME	SuperMAG	Auroral electrojet index (similar to AE)
SMU	SuperMAG	Upper auroral electrojet index (similar to AU)
SML	SuperMAG	Lower auroral electrojet index (similar to AL)
SymH	OMNI	Longitudinally symmetric H-component disturbance
AsyH	OMNI	Longitudinally asymmetric H-component disturbance
SymD	OMNI	Longitudinally symmetric D-component disturbance
AsyD	OMNI	Longitudinally asymmetric D-component disturbance
T	OMNI	Temperature
β	OMNI	Plasma beta
E	OMNI	Solar wind electric field
Proton Density	OMNI	Solar wind proton density
Flow Pressure	OMNI	Solar wind flow pressure
M_A	OMNI	Alfvén Mach number
M_s	OMNI	Magnetosonic Mach number
Clock Angle	OMNI	IMF clock angle
Cone Angle	OMNI	IMF cone angle
F10.7	OMNI	Solar flux at 10.7 cm wavelength
K_p	OMNI	K_p index

To compare the different features, the sklearn.feature_selection. SelectKBes function from scikit-learn (Pedregosa et al., 2011) was used to compare each parameter to the density, average ion mass and whether a measurement originated from within the PS or PT. This object uses a scoring function which determines how well changes in each feature correlate with changes in a given output parameter. Determining whether a point originates from the PS or PT populations is a classification problem, so the scoring function used for this was f_classif; but n_e and m_{av} are continuous variables, so the f_regression function was used in these cases. Both functions provide an "F-value," where a parameter with a larger F-value has more of an effect on the output parameter.

Figure B1 shows the feature analysis performed for (a) PS/PT classification, (b) n_e and (c) m_{av}. In all three panels, the most important feature (aside from L and density in panel a) is the SMR index, a measure of the

magnetic field deviation on the ground due to the variations in the Earth's ring current. The SMR index, like the D_{st} and SymH indices, are a useful indicator for the presence of geomagnetic storms which cause large enhancements in the Earth's ring current, resulting in negative deviations in SMR. It is therefore understandable that there is some correlation of SMR with electron densities and in particular with PS/PT classification because geomagnetic storms cause large changes in the structure of the plasmasphere though enhanced global convection, which results in an eroded plasmasphere (Moldwin et al., 2002) and the formation of a plume (e.g., Spasojević et al., 2003).

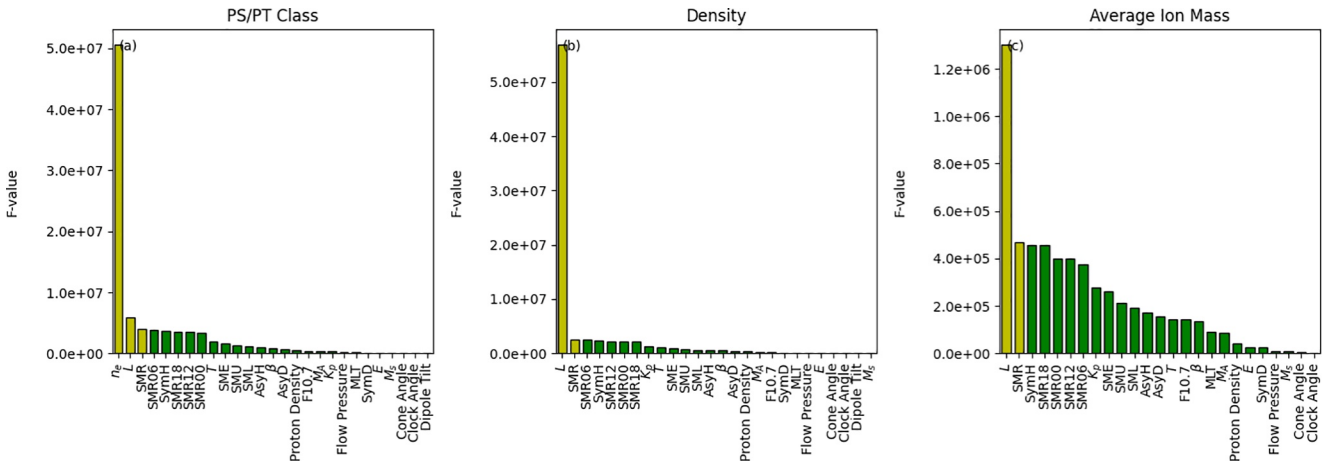

Figure B1. F-values for each potential feature parameter for (a) PS/PT classification, (b) electron density and (c) average ion mass. In each panel, parameters are sorted left to right from highest to lowest F-value, where the mean F-value is represented by a horizontal dashed line. Potential feature parameters include: SuperMAG ring current and electrojet indices; OMNI parameters such as solar wind velocity, dynamic pressure and IMF vectors; clock and cone angles derived from OMNI IMF vectors.

As a result of this feature analysis, the model parameters for all models will be parameterized by both L and SMR.

Appendix C: Network Architecture Selection and Training

In this section feed forward ANNs are used to predict the model parameters based on solar/geomagnetic activity. A feed forward ANN consists of nodes, analogous to neurons, which are arranged in layers; the first layer is the input layer, the final layer is the output layer, and the layers between are hidden layers. Each node has an activation function, which adds non-linearity to the ANN, the output of which is mapped to every node in the following layer. The ANN works by propagating input features through the ANN one layer at a time, until an output is produced.

For each of the four models presented in Sections 3, a single ANN is used to predict the axisymmetric, real and imaginary components of Equation 8. The input layers for every ANN used here contains just two nodes, one for L and one for SMR (P, PT and PS models). The output layer for every model contains 7 nodes: one for F_0, three for R_m and three for I_m (where m is 1, 2 or 3). With the exception of the output nodes, all nodes use the softplus function:

$$f(x) = \log_e(1 + e^x), \tag{C1}$$

which is a smooth approximation of the rectified linear unit (ReLU) (Glorot et al., 2011). The combination of ReLU units in the hidden layers adds the ability of the networks to form a highly non-linear model. The output nodes for the ANNs are linear, which means that they can output any real, finite value.

The specific configuration of a neural network (i.e., the number of layers, and number of nodes in each layer) is called the network "architecture." The exact numbers of hidden layers and nodes for each model

are initially unknowns, here they are determined by repeatedly training many different architectures and comparing the model outputs directly to the data collected by the Van Allen Probes.

Each network was constructed and trained using the Keras API (Chollet et al., 2015) in Python. The various ANN architectures used had 1 to 3 hidden layers, where each hidden layer consisted of 2–1024 nodes. The ANNs were each trained by minimizing the mean absolute error (MAE) cost function,

$$J = \frac{1}{n}\sum_{i=1}^{n} \mid \hat{y}^{(i)} - y^{(i)} \mid, \tag{C2}$$

using the Adam optimizer (Kingma & Ba, 2014), where n is the number of samples in each batch, i is the sample index, $\hat{y}^{(i)}$ is the predicted output value and y is the expected output value from the training samples. Training was performed in each case with mini-batches of 256 samples at a time (~ 1500 batches per epoch) for 250 epochs - a sufficiently high number of epochs for any further training progress to be negligible.

In order to test each architecture, a test set of data was compiled for each model. The test set was comprised of all of the data used in the initial L-S analysis in Section 3-L-shell, n_e, m_{av} and which population of plasma the spacecraft was in at each time, along with the associated SMR indices. During a test each ANN used the L and SMR index to predict the axisymmetric, real and imaginary components of a model at the positions of each probe, which were then used to calculate the relevant model output (i.e., m_{avPS}, n_{ePS}, etc.). The model output was then compared to the data using Equation C2 which provided a test set cost, J_{test}.

For each of the four models, every architecture was tested 20 times and the lowest J_{test} was recorded, where a low J_{test} signifies the a prediction which is closer to the measured data than a high J_{test}. The architectures with the best test costs were selected for the final model. Table C1 shows the numbers of hidden layers and the number of nodes in each layer for the best performing ANNs along with the total number of free parameters. The P and m_{av} models required the most complex ANN architectures with 3 hidden layers, each containing 4 nodes which corresponds to 87 free parameters; both density models were a little simpler with only 2 layers.

Table C1
Table Showing the Number of Hidden Layers, Nodes in Each Layer and the Total Number of Free Parameters in the Best Performing ANN Architectures for Each Model

Model	Hidden Layers	Nodes Per Layer	Free Parameters
P	3	4	87
n_{ePT}	2	2	33
n_{ePS}	2	5	63
m_{avPT}	3	4	87
m_{avPS}	3	4	87

Data Availability Statement

EMFISIS data are available at https://emfisis.physics.uiowa.edu/data/index. HOPE data are downloadable from https://www.rbsp-ect.lanl.gov/science/DataDirectories.php. The work by the EFW team was conducted under JHU/APL contract 922,613 (RBSP-EFW). EFW data are available from http://www.space.umn.edu/rbspefw-data/. The OMNI data were obtained from the GSFC/SPDF OMNIWeb interface at https://omniweb.gsfc.nasa.gov. The code for the SPICED model is available at https://github.com/mattkjames7/spicedmodel.

Acknowledgments
The work by Matthew K. James and Tim K. Yeoman is supported by STFC grant ST/H002480/1. The work by Jasmine K. Sandhu is supported by NERC grants NE/P017185/2 and NE/V002554/2. We gratefully acknowledge the SuperMAG collaborators (https://supermag.jhuapl.edu/info/?page=acknowledgement).The authors thank the people involved in providing the EMFISIS, HOPE and EFW data.

References

Alfvén, H. (1942). Existence of electromagnetic-hydrodynamic waves. *Nature*, *150*(3805), 405–406. https://doi.org/10.1038/150405d010.1038/150405d0

Bartels, J., Heck, N. H., & Johnston, H. F. (1939). The three-hour-range index measuring geomagnetic activity. *Terrestrial Magnetism and Atmospheric Electricity*, *44*(4), 411–454. https://doi.org/10.1029/te044i004p00411

Bergin, A., Chapman, S. C., & Gjerloev, J. W. (2020). AE, DST, and their SuperMAG counterparts: The effect of improved spatial resolution in geomagnetic indices. *Journal of Geophysical Research: Space Physics*, *125*(5), e2020JA027828. https://doi.org/10.1029/2020JA027828

Box, G. E., & Cox, D. R. (1964). An analysis of transformations. *Journal of the Royal Statistical Society*, *26*(2), 211–243. https://doi.org/10.1111/j.2517-6161.1964.tb00553.x

Carpenter, D. L. (1966). Whistler studies of the plasmapause in the magnetosphere: 1. Temporal variations in the position of the knee and some evidence on plasma motions near the knee. *Journal of Geophysical Research*, *71*(3), 693–709. https://doi.org/10.1029/jz071i003p00693

Carpenter, D. L., & Anderson, R. R. (1992). An ISEE/whistler model of equatorial electron density in the magnetosphere. *Journal of Geophysical Research: Space Physics*, *97*(A2), 1097–1108. https://doi.org/10.1029/91JA01548

Chappell, C. R. (1972). Recent satellite measurements of the morphology and dynamics of the plasmasphere. *Reviews of Geophysics*, *10*(4), 951–979. https://doi.org/10.1029/rg010i004p00951

Chollet, F., et al. (2015). *Keras*. https://keras.io

Chu, X., Bortnik, J., Li, W., Ma, Q., Denton, R., Yue, C., & Menietti, J. (2017). A neural network model of three-dimensional dynamic electron density in the inner magnetosphere. *Journal of Geophysical Research: Space Physics*, *122*(9), 9183–9197. https://doi.org/10.1002/2017ja024464

Cummings, W. D., O'Sullivan, R. J., & Coleman, P. J. (1969). Standing Alfvén waves in the magnetosphere. *Journal of Geophysical Research*, *74*(3), 778–793. https://doi.org/10.1029/ja074i003p00778

Darrouzet, F., Gallagher, D. L., André, N., Carpenter, D. L., Dandouras, I., Décréau, P. M. E., & Tu, J. (2009). Plasmaspheric density structures and dynamics: Properties observed by the cluster and image missions. *Space Science Reviews*, *145*(1), 55–106. https://doi.org/10.1007/s11214-008-9438-9

Décréau, P. M. E., Fergeau, P., Krannosels'kikh, V., Lévêque, M., Martin, P., Randriamboarison, O., & Mögensen, P. B. (1997). Whisper, a resonance sounder and wave analyser: Performances and perspectives for the cluster mission. *Space Science Reviews*, *79*(1), 157–193. https://doi.org/10.1023/A:1004931326404

Delport, B., Collier, A. B., Lichtenberger, J., Rodger, C. J., Parrot, M., Clilverd, M. A., & Friedel, R. H. W. (2012). Simultaneous observation of chorus and hiss near the plasmapause. *Journal of Geophysical Research: Space Physics*, *117*(A12), A12218. https://doi.org/10.1029/2012ja017609

Denton, R. E., Lessard, M. R., Anderson, R., Miftakhova, E. G., & Hughes, J. W. (2001). Determining the mass density along magnetic field lines from toroidal eigenfrequencies: Polynomial expansion applied to CRRES data. *Journal of Geophysical Research: Space Physics*, *106*(A12), 29915–29924. https://doi.org/10.1029/2001ja000204

Denton, R. E., Takahashi, K., Anderson, R. R., & Wuest, M. P. (2004). Magnetospheric toroidal Alfvén wave harmonics and the field line distribution of mass density. *Journal of Geophysical Research: Space Physics*, *109*(A6), A06202. https://doi.org/10.1029/2003JA010201

Denton, R. E., Takahashi, K., Thomsen, M. F., Borovsky, J. E., Singer, H. J., Wang, Y., & Reinisch, B. W. (2014). Evolution of mass density and o+ concentration at geostationary orbit during storm and quiet events. *Journal of Geophysical Research: Space Physics*, *119*(8), 6417–6431. https://doi.org/10.1002/2014ja019888

Funsten, H. O., Skoug, R. M., Guthrie, A. A., MacDonald, E. A., Baldonado, J. R., Harper, R. W., & Chen, J. (2013). Helium, oxygen, proton, and electron (hope) mass spectrometer for the radiation belt storm probes mission. *Space Science Reviews*, *179*(1), 423–484. https://doi.org/10.1007/s11214-013-9968-7

Gallagher, D. L., Craven, P. D., & Comfort, R. H. (1988). An empirical model of the earth's plasmasphere. *Advances in Space Research*, *8*(8), 15–24. https://doi.org/10.1016/0273-1177(88)90258-x

Gallagher, D. L., Craven, P. D., & Comfort, R. H. (2000). Global core plasma model. *Journal of Geophysical Research: Space Physics*, *105*(A8), 18819–18833. https://doi.org/10.1029/1999ja000241

Genestreti, K. J., Goldstein, J., Corley, G. D., Farner, W., Kistler, L. M., Larsen, B. A., & Turner, N. E. (2017). Temperature of the plasmasphere from Van Allen probes hope. *Journal of Geophysical Research: Space Physics*, *122*(1), 310–323. https://doi.org/10.1002/2016ja023047

Gjerloev, J. W. (2012). The SuperMAG data processing technique. *Journal of Geophysical Research: Space Physics*, *117*(A9). https://doi.org/10.1029/2012ja017683

Glauert, S. A., & Horne, R. B. (2005). Calculation of pitch angle and energy diffusion coefficients with the PADIE code. *Journal of Geophysical Research: Space Physics*, *110*(A4). https://doi.org/10.1029/2004ja010851

Glorot, X., Bordes, A., & Bengio, Y. (2011). Deep sparse rectifier neural networks. In *Proceedings of the fourteenth international conference on artificial intelligence and statistics* (pp. 315–323).

Goldstein, J., Burch, J. L., & Sandel, B. R. (2005). Magnetospheric model of subauroral polarization stream. *Journal of Geophysical Research: Space Physics*, *110*(A9). https://doi.org/10.1029/2005ja011135

Goldstein, J., Gallagher, D., Craven, P. D., Comfort, R. H., Genestreti, K. J., Mouikis, C., & De Pascuale, S. (2019). Temperature dependence of plasmaspheric ion composition. *Journal of Geophysical Research: Space Physics*, *124*(8), 6585–6595. https://doi.org/10.1029/2019ja026822

Goldstein, J., Hudson, M. K., & Lotko, W. (1999). Possible evidence of damped cavity mode oscillations stimulated by the January, 1997 magnetic cloud event. *Geophysical Research Letters*, *26*(24), 3589–3592. https://doi.org/10.1029/1999gl003636

Goldstein, J., Pascuale, S. D., Kletzing, C., Kurth, W., Genestreti, K. J., Skoug, R. M., & Spence, H. (2014). Simulation of van allen probes plasmapause encounters. *Journal of Geophysical Research: Space Physics*, *119*(9), 7464–7484. https://doi.org/10.1002/2014ja020252

Hocke, K. (1998). Phase estimation with the lomb-scargle periodogram method. *Annales Geophysicae*, *16*, 356–358.

King, J. H., & Papitashvili, N. E. (2005). Solar wind spatial scales in and comparisons of hourly wind and ace plasma and magnetic field data. *Journal of Geophysical Research: Space Physics*, *110*(A2). https://doi.org/10.1029/2004ja010649

Kingma, D. P., & Ba, J. (2014). *Adam: A method for stochastic optimization*.

Kletzing, C. A., Kurth, W. S., Acuna, M., MacDowall, R. J., Torbert, R. B., Averkamp, T., & Tyler, J. (2013). The electric and magnetic field instrument suite and integrated science (EMFISIS) on RBSP. *Space Science Reviews*, *179*(1), 127–181. https://doi.org/10.1007/s11214-013-9993-6

Kronberg, E. A., Ashour-Abdalla, M., Dandouras, I., Delcourt, D. C., Grigorenko, E. E., Kistler, L. M., & Zelenyi, L. M. (2014). Circulation of heavy ions and their dynamical effects in the magnetosphere: Recent observations and models. *Space Science Reviews*, *184*(1), 173–235. https://doi.org/10.1007/s11214-014-0104-0

Lomb, N. R. (1976). Least-squares frequency analysis of unequally spaced data. *Astrophysics and Space Science*, *39*(2), 447–462. https://doi.org/10.1007/BF00648343

Mauk, B. H., Fox, N. J., Kanekal, S. G., Kessel, R. L., Sibeck, D. G., & Ukhorskiy, A. (2013). Science objectives and rationale for the radiation belt storm probes mission. *Space Science Reviews*, *179*(1), 3–27. https://doi.org/10.1007/s11214-012-9908-y

Miyoshi, Y., Kasaba, Y., Shinohara, I., Takashima, T., Asamura, K., Matsumoto, H., et al. (2017). Geospace exploration project: Arase (ERG). *Journal of Physics: Conference Series*, *869*, 012095. https://doi.org/10.1088/1742-6596/869/1/012095

Moldwin, M. B., Downward, L., Rassoul, H. K., Amin, R., & Anderson, R. R. (2002). A new model of the location of the plasmapause: CRRES results. *Journal of Geophysical Research: Space Physics*, *107*(A11), SMP 2-1–SMP 2-9. https://doi.org/10.1029/2001ja009211

Nelder, J. A., & Mead, R. (1965). A simplex method for function minimization. *Computer Journal*, *7*(4), 308–313. https://doi.org/10.1093/comjnl/7.4.308

Newell, P. T., & Gjerloev, J. W. (2011). Evaluation of SuperMAG auroral electrojet indices as indicators of substorms and auroral power. *Journal of Geophysical Research: Space Physics*, *116*(A12), A12211. https://doi.org/10.1029/2011JA016779

Newell, P. T., & Gjerloev, J. W. (2012). SuperMAG-based partial ring current indices. *Journal of Geophysical Research: Space Physics*, *117*(A5), A05215. https://doi.org/10.1029/2012ja017586

Nosé, M., Matsuoka, A., Kumamoto, A., Kasahara, Y., Goldstein, J., Teramoto, M., & MacDowall, R. J. (2018). Longitudinal structure of oxygen torus in the inner magnetosphere: Simultaneous observations by Arase and Van Allen probe A. *Geophysical Research Letters*, *45*(19), 10177–10184. https://doi.org/10.1029/2018gl080122

Pedregosa, F., Varoquaux, G., Gramfort, A., Michel, V., Thirion, B., Grisel, O., & Duchesnay, E. (2011). Scikit-learn: Machine learning in Python. *Journal of Machine Learning Research*, *12*, 2825–2830.

Phan, T. D., Paschmann, G., Gosling, J. T., Oieroset, M., Fujimoto, M., Drake, J. F., & Angelopoulos, V. (2013). The dependence of magnetic reconnection on plasma β and magnetic shear: Evidence from magnetopause observations. *Geophysical Research Letters*, *40*(1), 11–16. https://doi.org/10.1029/2012gl054528

Radoski, H. R., & Carovillano, R. L. (1966). Axisymmetric plasmasphere resonances: Toroidal mode. *The Physics of Fluids*, *9*(2), 285–291. https://doi.org/10.1063/1.1761671

Rème, H., Bosqued, J. M., Sauvaud, J. A., Cros, A., Dandouras, J., Aoustin, C., & Balsiger, H. (1997). The cluster ion spectrometry (CIS) experiment. In C. P. Escoubet, C. T. Russell, & R. Schmidt (Eds.), *The cluster and phoenix missions* (pp. 303–350). Springer Netherlands. https://doi.org/10.1007/978-94-011-5666-0_12

Roberts, W. T., Horwitz, J. L., Comfort, R. H., Chappell, C. R., Waite, J. H., & Green, J. L. (1987). Heavy ion density enhancements in the outer plasmasphere. *Journal of Geophysical Research: Space Physics*, *92*(A12), 13499–13512. https://doi.org/10.1029/JA092iA12p13499

Russell, C. T., Holzer, R. E., & Smith, E. J. (1969). Ogo 3 observations of elf noise in the magnetosphere: 1. spatial extent and frequency of occurrence. *Journal of Geophysical Research (1896-1977)*, *74*(3), 755–777. https://doi.org/10.1029/ja074i003p00755

Sandhu, J. K., Yeoman, T. K., Fear, R. C., & Dandouras, I. (2016). A statistical study of magnetospheric electron density using the cluster spacecraft. *Journal of Geophysical Research: Space Physics*, *121*(11), 11–11. https://doi.org/10.1002/2016ja023397

Sandhu, J. K., Yeoman, T. K., Fear, R. C., & Dandouras, I. (2016). A statistical study of magnetospheric ion composition along the geomagnetic field using the cluster spacecraft for l values between 5.9 and 9.5. *Journal of Geophysical Research: Space Physics*, *121*(3), 2194–2208. https://doi.org/10.1002/2015ja022261

Sandhu, J. K., Yeoman, T. K., Rae, I. J., Fear, R. C., & Dandouras, I. (2017). The dependence of magnetospheric plasma mass loading on geomagnetic activity using cluster. *Journal of Geophysical Research: Space Physics*, *122*(9), 9371–9395. https://doi.org/10.1002/2017ja024171

Scargle, J. (1983). Studies in astronomical time series analysis. II - Statistical aspects of spectral analysis of unevenly spaced data. *The Astrophysical Journal*, *263*. https://doi.org/10.1086/160554

Sheeley, B. W., Moldwin, M. B., Rassoul, H. K., & Anderson, R. R. (2001). An empirical plasmasphere and trough density model: Crres observations. *Journal of Geophysical Research: Space Physics*, *106*(A11), 25631–25641. https://doi.org/10.1029/2000ja000286

Spasojević, M., Goldstein, J., Carpenter, D. L., Inan, U. S., Sandel, B. R., Moldwin, M. B., & Reinisch, B. W. (2003). Global response of the plasmasphere to a geomagnetic disturbance. *Journal of Geophysical Research: Space Physics*, *108*(A9), 1340. https://doi.org/10.1029/2003JA009987

Spence, H. E., Reeves, G. D., Baker, D. N., Blake, J. B., Bolton, M., Bourdarie, S., & Thorne, R. M. (2013). Science goals and overview of the radiation belt storm probes (RBSP) energetic particle, composition, and thermal plasma (ECT) suite on NASA's Van Allen probes mission. *Space Science Reviews*, *179*(1), 311–336. https://doi.org/10.1007/s11214-013-0007-5

Stern, D. P. (1975). The motion of a proton in the equatorial magnetosphere. *Journal of Geophysical Research (1896-1977)*, *80*(4), 595–599. https://doi.org/10.1029/ja080i004p00595

Takahashi, K., Denton, R. E., Anderson, R. R., & Hughes, W. J. (2004). Frequencies of standing Alfvén wave harmonics and their implication for plasma mass distribution along geomagnetic field lines: Statistical analysis of CRRES data. *Journal of Geophysical Research: Space Physics*, *109*(A8). https://doi.org/10.1029/2003JA010345

Takahashi, K., Denton, R. E., Anderson, R. R., & Hughes, W. J. (2006). Mass density inferred from toroidal wave frequencies and its comparison to electron density. *Journal of Geophysical Research: Space Physics*, *111*(A1). https://doi.org/10.1029/2005ja011286

Takahashi, K., Ohtani, S.-i., Denton, R. E., Hughes, W. J., & Anderson, R. R. (2008). Ion composition in the plasma trough and plasma plume derived from a combined release and radiation effects satellite magnetoseismic study. *Journal of Geophysical Research: Space Physics*, *113*(A12). https://doi.org/10.1029/2008ja013248

Trotignon, J. G., Décréau, P. M. E., Rauch, J. L., Randriamboarison, O., Krasnoselskikh, V., Canu, P., & Fergeau, P. (2001). How to determine the thermal electron density and the magnetic field strength from the cluster/whisper observations around the earth. *Annales Geophysicae*, *19*(10/12), 1711–1720. https://doi.org/10.5194/angeo-19-1711-2001

Trotignon, J. G., Rauch, J. L., Décréau, P. M. E., Canu, P., & Lemaire, J. (2003). Active and passive plasma wave investigations in the earth's environment: The cluster/whisper experiment. *Advances in Space Research*, *31*(5), 1449–1454. https://doi.org/10.1016/S0273-1177(02)00959-6

Usanova, M. E., Mann, I. R., Rae, I. J., Kale, Z. C., Angelopoulos, V., Bonnell, J. W., & Singer, H. J. (2008). Multipoint observations of magnetospheric compression-related EMIC Pc1 waves by THEMIS and CARISMA. *Geophysical Research Letters*, *35*(17). https://doi.org/10.1029/2008gl034458

Volland, H. (1973). A semiempirical model of large-scale magnetospheric electric fields. *Journal of Geophysical Research (1896-1977)*, *78*(1), 171–180. https://doi.org/10.1029/ja078i001p00171

Wharton, S. J., Rae, I. J., Sandhu, J. K., Walach, M.-T., Wright, D. M., & Yeoman, T. K. (2020). The changing eigenfrequency continuum during geomagnetic storms: Implications for plasma mass dynamics and ULF wave coupling. *Journal of Geophysical Research: Space Physics*, *125*(6), e2019JA027648. https://doi.org/10.1029/2019JA027648

Wharton, S. J., Wright, D. M., Yeoman, T. K., James, M. K., & Sandhu, J. K. (2018). Cross-phase determination of ultralow frequency wave harmonic frequencies and their associated plasma mass density distributions. *Journal of Geophysical Research: Space Physics*, *123*(8), 6231–6250. https://doi.org/10.1029/2018ja025487

Wygant, J. R., Bonnell, J. W., Goetz, K., Ergun, R. E., Mozer, F. S., Bale, S. D., & Tao, J. B. (2013). The electric field and waves instruments on the radiation belt storm probes mission. *Space Science Reviews*, *179*(1), 183–220. https://doi.org/10.1007/s11214-013-0013-7

Zhelavskaya, I. S., Shprits, Y. Y., & Spasojević, M. (2017). Empirical modeling of the plasmasphere dynamics using neural networks. *Journal of Geophysical Research: Space Physics*, *122*(11), 11227–11244. https://doi.org/10.1002/2017ja024406